



OPEN A nonlinear observer-based control strategy for hybrid energy storage systems to improve voltage disturbance rejection in DC microgrids

Syphax Ihammouchen¹, Ali Chebabhi², Djamel Ziane³, Toufik Rekioua¹, Mohamed Fouad Benkhoris³, Youcef Belkhier⁴, Mohit Bajaj^{5,6,7}✉ & Olena Rubanenko⁸✉

This paper proposes an efficient nonlinear observer-based a simple and effective control approach for DC microgrids integrating hybrid energy storage systems (HESs) composed of supercapacitors and batteries with photovoltaic (PV) generation. The study focuses on improving HESS performance in DC microgrids, particularly in achieving fast and accurate DC microgrid bus voltage control, improved dynamic response, enhanced disturbance rejection capabilities, and better HESS power allocation. The proposed scheme combines a proportional–integral (PI) voltage controller with a variable-gain Nonlinear High-Gain Observer (NHGO) that estimates and compensates external disturbances, including load changes and PV power fluctuations. Unlike conventional high-gain or extended-state observers, which negatively impacted by measurement noise that can only be mitigated by reducing observer gain, consequently weakening dynamic response, the NHGO overcomes this limitation by dynamically adjusts its gain to achieve fast disturbance estimation during transients while maintaining noise immunity in steady state. This is achieved by utilizing high gain values during transient states for rapid disturbance estimation and rejection, followed by gain reduction during steady state to minimize noise and estimation error. Accordingly, the control strategy strategically allocates power demands between battery and supercapacitor storage components based on their inherent characteristics, effectively managing both transient and steady-state power imbalances while maintaining stable DC microgrid bus voltage. The complete system was implemented and validated through MATLAB/Simulink and real-time experiments using the OP5700 simulator. Results prove up to 45% reduction in voltage overshoot, 35% improvement in settling time, and superior robustness against parameter variations compared with ESO-LPF, HGO-LPF, and STO-LPF based control methods.

Keywords Photovoltaic, DC microgrid, Hybrid energy storage systems, Energy management system, Non-linear high gain observer, Integral-backstepping MPPT, DC microgrid bus voltage stability

Due to the proliferation of renewable energy sources (RESs), significant advances in energy storage technologies, increased use of direct current (DC) loads, and multiple benefits inherent in DC power distribution, DC microgrids are emerging as an essential paradigm in modern power systems¹. They have shown exceptional reliability and resilience in integrating and managing renewable energy sources while supporting critical loads^{2,3}. In contrast to their AC counterparts, these systems exhibit a less intricate structure, especially concerning the stages of power conversion and control mechanisms^{4,5}.

¹Faculté de Technologie, Laboratoire de Technologie Industrielle et de l'Information (LTII), Université de Bejaia, Bejaia 06000, Algeria. ²Electrical Engineering Laboratory, University of M'sila University, Pole, Road Bourdj Bou Arreiridj, M'sila 28000, Algeria. ³IREENA Laboratory, University of Nantes, Saint-Nazaire, France. ⁴University of Brest, UMR CNRS 6027, Brest 29238, France. ⁵Department of Electrical Engineering, Graphic Era (Deemed to be University), Dehradun 248002, India. ⁶Hourani Center for Applied Scientific Research, Al-Ahliyya Amman University, Amman, Jordan. ⁷Graphic Era Hill University, Dehradun 248002, India. ⁸Department of Power Plants and System, Vinnytsia National Technical University, Vinnytsia 21000, Ukraine. ✉email: mohitbajajphd@gmail.com; olenarubanenko@vntu.edu.ua

In modern DC microgrid architectures, HESSs are indispensable components⁶. Indeed, they provide an excellent ability to overcome failures and enhance dynamic responses in both stable and transient conditions, thereby strengthening the resilience of these microgrid systems^{6,7}. The most common HESS configuration combines a battery and supercapacitor, forming a synergistic system^{3,8}. This combination enables optimal power management and superior performance by leveraging its distinctive characteristics, including high energy and power densities^{9,10}. It also guarantees a long-term energy supply and rapid response to transient power fluctuation demands^{11,12}. Nevertheless, HESSs often encounter variable operating conditions and numerous technical challenges⁹. In addition, the characteristics of power generation systems degrade over time, presenting complex challenges for designing control structures and maintaining system stability^{13,14}. To meet these challenges, advanced solutions that address power imbalances, ensure optimal regulation of the DC microgrid bus voltage, and enhance the ability to reject disturbances during transient and steady-state conditions are essential.

The method based on PI compensators is one of the most frequently used methods for dealing with these challenges^{15,16}. However, this technique only allows the rejection of basic disturbances, and its performance deteriorates under variable operating conditions or with uncertain parameters. Some studies have introduced an additional control loop based on active damping to resolve stability problems and oscillations caused by associated static converters and load variations, including the virtual capacitance loop¹⁵ and the virtual resistance loop¹⁷. Nevertheless, its implementation is complex, and coupled disturbances strongly influence the system's dynamic behavior. To address these coupled disturbances, sliding-mode control techniques are employed, which guarantee robust performance. However, chattering phenomena can occur in the case of uncoupled disturbances¹⁸.

Since traditional methods often present limitations and do not allow for the simultaneous rejection of disturbances from various sources, developing more advanced control solutions is necessary. To this end, several control strategies have been proposed, including Feedforward compensation techniques based on direct sensor measurements used in^{6,19,20} to mitigate voltage fluctuations in microgrids. However, the accuracy of disturbance modeling and the precision of measurements significantly influence the effectiveness of sustaining DC microgrid bus voltage dynamics^{14,21,22}. Moreover, the need for supplementary sensors increases the potential for measurement inaccuracies, raises costs and power losses, and could jeopardize the system's integrity.

On the other hand, state observer-based control approaches have recently attracted considerable interest in controlling DC microgrids. Although Luenberger²³ and sliding mode observers^{24,25} have demonstrated their effectiveness in maintaining DC microgrid bus voltage stability and their ability to reject disturbances, their accuracy against HESS, whose components operate on distinct time scales, can be affected by parameter variations and model uncertainties due to the different characteristics of HESS components. To address the issues related to fluctuations in photovoltaic output power, load variations, and DC microgrid bus voltage variations in HESS-based DC microgrids, a deadbeat control method based on enhanced linear state observers (ELSO) was proposed in²⁶. Although this technique provides enhanced system reliability, good DC microgrid bus voltage dynamics performance, and improved disturbance rejection, its bandwidth in practical applications remains limited. A very high bandwidth allows for rapid convergence but also generates significant noise, which is harmful to the system's performance and a major concern.

A type-2 fuzzy approach based on extended state observer (ESO) was developed in²⁷ to provide robust control and energy management for HESS in DC microgrids. This solution utilizes ESO to estimate and compensate for unknown disturbances and system uncertainties while enhancing robustness against parameter variations due to type-2 fuzzy logic²⁸. However, alongside the drawbacks of ESO and the computational complexity imposed by the type-2 fuzzy controller, this technique necessitates meticulous parameter tuning to ensure system stability during rapid power transitions²⁷. Kalman filters have also been investigated for HESS control²⁹. They enable sophisticated state estimation. However, as batteries and supercapacitors operate on different time scales, the precision of these estimators may be adversely affected during rapid transients. The authors of¹⁸ proposed a fast composite backstepping control (FCBC)-based high-order sliding mode observer (HOSMO) for controlling HESS in microgrids^{30,31}. This combined approach takes advantage of HOSMO's ability to estimate and compensate for disturbances, while FCBC ensures rapid convergence and superior transient response. Although this solution demonstrates significant resilience to system uncertainties and external disturbances, higher-order terms and the composite control law complicate the calculations and tuning of parameters, along with stability-related challenges.

Generally, conventional observers often struggle to achieve efficient disturbance rejection while maintaining an excellent dynamic response and effective noise suppression when controlling HESS-based microgrids under varying operating conditions. To this end, multiple observers have been developed to overcome these limitations, including super-twisting disturbance observer^{31–33}, adaptive super-twisting extended state observer³⁴, high-gain observer (HGO)³⁵, and nonlinear high-gain observer (NHGO)^{36,37}. Among these advanced observers, the NHGO is a promising solution for HESS-based microgrids due to its simple design, ease of parameter tuning, and ability to efficiently resolve the traditional trade-off between rapid state estimation convergence and noise attenuation capabilities. In addition, this observer relies on an adaptive gain mechanism that uses high gain values to ensure rapid disturbance estimation and rejection during transient conditions and lower gain values to reduce measurement noise sensitivity and minimize estimation errors in a steady state while retaining effective disturbance rejection properties.

This paper a NHGO is proposed to address the microgrid voltage regulation and HESS power allocation challenges in PV/battery/supercapacitor-based DC microgrids. The proposed NHGO enables excellent estimation of the PV and load powers, enabling batter feedforward compensation in the microgrid voltage control loop. It is specifically designed to observe disturbances influencing the microgrid voltage, including load variations and PV power fluctuations. By doing so, the proposed NHGO enhances control performance and DC microgrid bus voltage disturbance rejections, ensuring robust operation, fast transient dynamics, stable

voltage regulation, HESS power allocation, and reduced measurement noise under diverse operating conditions by its accurate and fast disturbance estimations. Furthermore, instead of directly controlling the measured DC microgrid bus voltage, this paper adopts the observed DC microgrid bus voltage state as the control variable and regulated it with its reference in the DC microgrid bus voltage control loop, generating current references for the battery and supercapacitor control loops to enhance HESS power allocation, steady-state performance, and reduce measurement noise. On the other hand, in this paper, the maximum power point of the PV system is achieved through a hybrid maximum power point tracking (MPPT) technique that combines the Incremental Conductance (InC) algorithm with integral backstepping control. This combination reduces steady-state errors and overshoot, thereby improving the efficiency of the PV system. The proposed control scheme outperforms existing methods under various operating conditions by achieving an optimal balance between measurement noise immunity and disturbance rejection capability. It exhibits minimal steady-state estimation error, excellent DC microgrid bus voltage dynamics, improved power point tracking, and significantly enhanced HESS component lifespan. The effectiveness of the proposed strategy is validated through real-time simulations using the OPAL-RT OP5700 platform.

This paper is organized as follows: Section II provides a comprehensive analysis and modeling of the DC microgrid system. Section III presents the proposed control approach, incorporating NHGO-LPF for hybrid storage system control and hybrid MPPT for PV system control. Section 4 covers the simulation results and real-time validation of the proposed approach, followed by the conclusion in Sect. 5.

System description and modeling

This section provides an overview of the standalone DC microgrid system under investigation. As illustrated in Fig. 1, the proposed system consists of a photovoltaic (PV) panel connected to a fully active hybrid energy storage system (HESS) that includes both a battery and a supercapacitor. The PV panel is connected to the DC microgrid bus via a DC–DC boost converter (BC), while both the battery and the supercapacitor are individually connected to the DC microgrid bus through bidirectional DC–DC converters (BDDCs).

All components are interconnected through a unified DC microgrid bus, enhancing the overall resilience of the system. The microgrid is designed to meet the power demands of applications in remote areas where access to the main power grid is unavailable. Additionally, in this section, the dynamic models of all elements in the DC microgrid are presented. First, the dynamic model of the BC coupled with the solar PV unit is developed. Next, the dynamic model of the battery with its BDDC is derived. Finally, the dynamic model of the supercapacitor with its BDDC is formulated.

PV with BC system modeling

A photovoltaic cell consists of two layers of semiconductor materials that are doped differently, creating a P-N junction. When exposed to sunlight, if the photon energy exceeds the bandgap, a photocurrent is generated with an intensity proportional to solar irradiation. Numerous mathematical models for PV cells are available in the literature. Due to its simplicity and accuracy, the R-Shunt single-diode model is used in this study. As shown in Fig. 2, this model comprises a series resistance (R_s) and a parallel resistance (R_{sh}), representing the losses due to contact resistance between the silicon and electrode surfaces, as well as the leakage current in the P-N junction.

The equations governing the PV one-diode model are as follows^{38,39}:

$$i_{pv0} = i_{ph} - i_0 \left[\exp \left(\frac{v_{pv} - R_s \cdot i_{pv0}}{\alpha v_{th}} \right) - 1 \right] - \left(\frac{v_{pv} - R_s \cdot i_{pv0}}{R_{sh}} \right) \tag{1}$$

$$i_{Ph} = (i_{pvSTC} + k_i \cdot \Delta T) \frac{G}{G_{STC}} \tag{2}$$

$$V_{th} = \left(\frac{N_s \cdot K \cdot T}{q} \right) \tag{3}$$

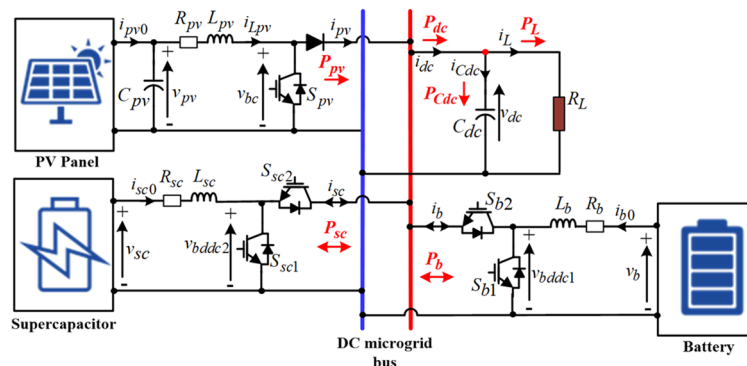


Fig. 1. Overall DC microgrid system architecture.

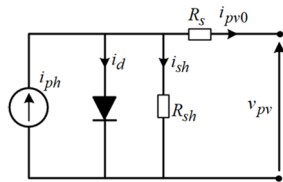


Fig. 2. Single diode model of PV module.

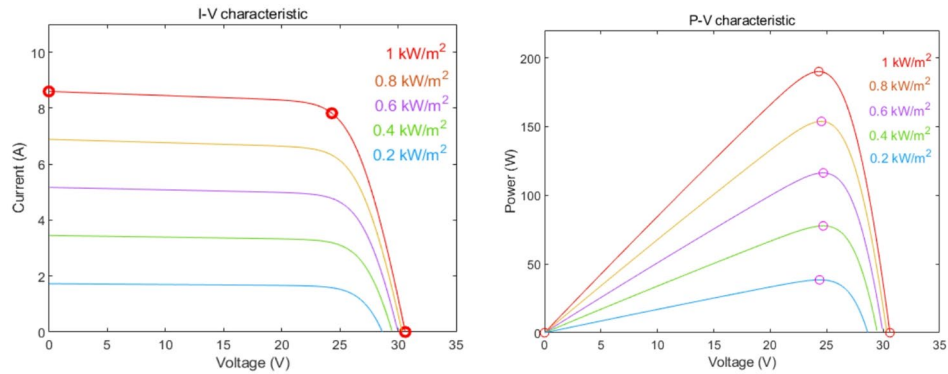


Fig. 3. I-V and P-V characteristics under different irradiances.

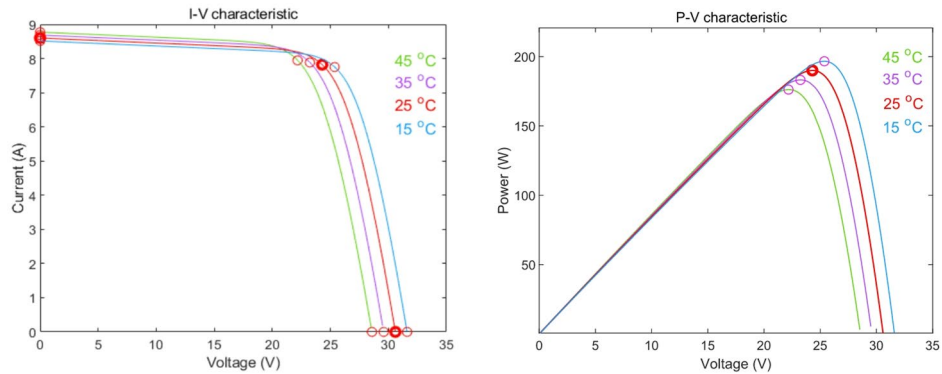


Fig. 4. I-V and P-V characteristics under different temperatures.

$$i_0 = \frac{i_{sc} + K \cdot \Delta T}{\exp\left(v_{oc} + \frac{k_v \cdot \Delta T}{\alpha \cdot v_{th}}\right)} \tag{4}$$

where v_{pv} denotes the PV output voltage (V), and i_{pv0} denotes the PV output current (A), α is the diode ideality factor, k_i and k_v are the current and voltage coefficients respectively, ΔT is the difference between the real temperature and the temperature at STC conditions, G and G_{STC} are respectively the actual irradiation and the irradiation at STC conditions, N_s represents the number of cells in series, K is the Boltzmann constant, the absolute value of the electron’s charge is denoted q , v_{oc} is the open circuit voltage, and i_{sc} represents the short-circuit current.

Figure 3 illustrates PV characteristics at a constant temperature of 25 °C under variable irradiation conditions, demonstrating that solar irradiation directly impacts the current of the photovoltaic panel and, consequently, its output power. Figure 4 illustrates the results obtained under varying temperature conditions while maintaining a constant irradiation level of 1000 W/m². It is clear that while temperature variations do not affect the current, they decrease the output voltage of the photovoltaic module.

The PV with BC serves as the primary power source in the DC microgrid system, responsible for both power generation and voltage regulation. The BC is controlled to regulate the PV output for extract maximum available power from the solar panels under varying irradiance, temperature, and loading conditions while simultaneously stepping down the PV voltage to match the voltage level required by the microgrid. Through the

BC control system that controls the duty cycle based on the dynamics of the PV output voltage and BC input current, this configuration manages the power injection from the PV into the DC microgrid bus, ensuring stable operation. In the typical energy management hierarchy of this DC microgrid architecture, the PV-BC acts as the primary energy source when solar irradiance is available, while the battery serves as a secondary source for sustained power during low or no solar conditions, and the supercapacitor functions as a fast-response energy buffer for transient power demands and power quality improvement. The PV-BC thus acts as the foundation of the energy supply chain, with the battery and supercapacitor providing complementary energy storage and power smoothing functions to serve the connected loads.

Throughout the following, we will assume that the Boost converter operates in continuous conduction mode (CCM). Two operating periods can be determined depending on whether the switch ‘S’ in the BC is ‘ON’ or ‘OFF’. Form this and applying Kirchhoff’s law to the system shown in Fig. 2, the dynamics of the PV output voltage ($\frac{dv_{pv}}{dt}$) and the BC input current ($\frac{di_{Lpv}}{dt}$) are given in Eq. (99)⁴⁰:

$$\begin{cases} \frac{dv_{pv}}{dt} = \frac{1}{C_{pv}} i_{C_{pv}} = \frac{1}{C_{pv}} (i_{pv0} - i_{Lpv}) \\ \frac{di_{Lpv}}{dt} = \frac{1}{L_{pv}} (v_{Lpv} - R_{pv} i_{Lpv}) = \frac{1}{L_{pv}} (v_{pv} - R_{pv} i_{Lpv} - (1 - D_{pv})v_{dc}) \end{cases} \quad (5)$$

where C_{pv} denotes the PV output capacitor (F), $i_{C_{pv}}$ is the PV output capacitor current (A), i_{Lpv} is the BC input current (A), L_{pv} is the BC input filter inductance (H) and v_{Lpv} is the droop voltage across this inductance (V), R_{pv} is the internal resistance of L_{pv} (Ω), D_{pv} is the duty cycle of the BC, and v_{dc} is the DC microgrid bus voltage (V).

The dynamics of the PV output voltage and the BC input current in Eq. (99) are used to control the PV-BC system using the integral backstepping (IBSC) to provide the duty cycle of the BC D_{pv} , as presented in Sect. 4.

Battery modeling

The electrical model that characterizes a Li-ion battery is shown in Fig. 5⁴¹.

The battery voltage equations are given as follow:

$$E = v_{b0} - k \frac{Q}{Q - \int i_{b0} dt} + A \cdot e^{(-B \int i_{b0} dt)} \quad (6)$$

$$v_b = v_{b0} - R_{b0} i_{b0} \quad (7)$$

where R_{b0} is the internal battery resistance, Q represents the maximum battery capacitance, A is exponential voltage and i_{b0} is the battery current.

To design an efficient energy management system, it is crucial to understand the different performance characteristics of the battery used. Figure 6 shows the discharge characteristics of a Li-ion battery. Generally, the discharge behavior of the battery can be divided into three zones.

- Exponential zone (yellow): This phase corresponds to the initial exponential voltage drop, starting from the fully charged state. It depends mainly on the battery’s composition and the operating conditions.
- Nominal zone (gray): This is the main operating range, where the voltage remains relatively stable around the nominal value.
- Total discharge zone: This phase is marked by a rapid voltage drop and must be avoided during operation to preserve the battery’s state of health.

Supercapacitor modeling

This supercapacitor model employs a modified Stern equation to characterize the nonlinear relationship between charge and voltage. As shown in Fig. 7, the model considers both normal operation and self-discharge phenomena through a dual-current approach governed by a switching function⁴².

The supercapacitor current and voltage output are defined as follows:

$$i = i_{sc} (1 - u(t)) + i_{selfdis} u(t) \quad (8)$$

$$v_{sc} = v_T - R_{sc} I_{sc} \quad (9)$$

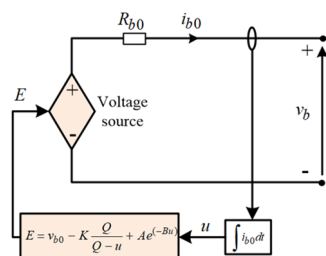


Fig. 5. Lithium-ion type battery model.

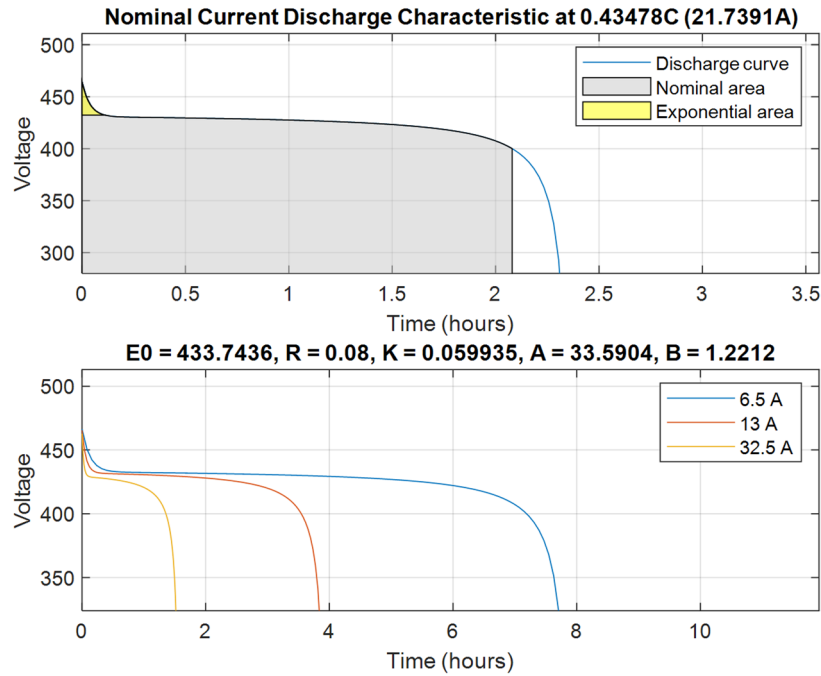


Fig. 6. Lithium-ion battery characteristics.

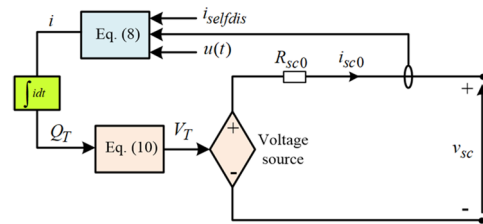


Fig. 7. Supercapacitor model.

where

$$v_T = \frac{N_s Q_T d}{N_p N_e \epsilon \epsilon_0 A_i} + \frac{2 N_e N_s R T}{F} \operatorname{asinh} \left(\frac{Q_T}{N_p N_e^2 A_i \sqrt{8 R T \epsilon \epsilon_0 c}} \right) \tag{10}$$

HESS with BDDCs modeling

As illustrated in Fig. 1, two bidirectional DC–DC converters (BDDCs) are employed to enable proper interfacing between the battery/supercapacitor-based hybrid energy storage system (HESS) and the DC microgrid. These converters regulate the bidirectional flow of power, operating in both buck and boost modes as required. the HESS plays a pivotal role in ensuring continuous and stable power delivery to the DC load. The battery, characterized by high energy density, provides sustained energy support and compensates for long-term power imbalances. Meanwhile, the supercapacitor, with its superior power density and fast response, mitigates short-term fluctuations and transient load variations. By means of coordinated control of their respective BDDCs, the battery and supercapacitor manage bidirectional power flow with the DC microgrid bus, thereby stabilizing the system voltage. During periods of excess PV generation, surplus energy is used to charge the storage units, whereas under low solar output or sudden load changes, the HESS discharges to maintain power balance. This cooperative operation among the PV system, HESS, and DC load enhances the dynamic response, reliability, and overall efficiency of the DC microgrid. By applying the Kirchhoff’s laws to the battery and supercapacitor HESS together with their respective BDDCs, as depicted in Fig. 1, the dynamic equations governing the DC microgrid voltage ($\frac{dv_{dc}}{dt}$), BDDC-based battery input current ($\frac{di_{b0}}{dt}$), and the BDDC-based battery input current ($\frac{di_{sc0}}{dt}$) are given in Eq.(11)⁴⁰:

$$\begin{cases} \frac{dv_{dc}}{dt} = \frac{1}{C_{dc}} i_{Cdc} = \frac{1}{C_{dc}} (i_{pv} + i_b + i_{sc} - i_L) \\ \frac{di_{b0}}{dt} = \frac{1}{L_b} (v_b - R_b i_{b0} - v_{dc} - D_b v_{dc}) \\ \frac{di_{sc0}}{dt} = \frac{1}{L_{sc}} (v_{sc} - R_{sc} i_{sc0} - v_{dc} - D_{sc} v_{dc}) \end{cases} \quad (11)$$

where i_b and i_{sc} are the output currents of the BDDC-based battery system and BDDC-based supercapacitor system in (A), respectively.

By applying the power balance principle among the input and output of each BDDC within the HESS, we obtained the relation between the each BDDC input and output current as follows:

$$\begin{cases} i_b = \frac{v_{bdc1}}{v_{dc}} i_{b0} \\ i_{sc} = \frac{v_{bdc2}}{v_{dc}} i_{sc0} \end{cases} \quad (12)$$

where v_{bdc1} is the BDDC-based battery system input voltage (V) and v_{bdc2} is the BDDC-based supercapacitor system input voltage (V).

Substituting the currents in Eq.(12) into the DC microgrid voltage dynamics in Eq.(11), we have

$$\frac{dv_{dc}}{dt} = \frac{1}{C_{dc}} i_{Cdc} = \frac{1}{C_{dc}} \left(i_{pv} + \frac{v_{bdc1}}{v_{dc}} i_{b0} + \frac{v_{bdc2}}{v_{dc}} i_{sc0} - i_L \right) \quad (13)$$

This equation allows for the determination of the reference currents of both the inner battery current control loop and inner supercapacitor current control loop via low pass filter, in which the low-frequency component of the reference current provided from the regulation if the DC microgrid regulation is assigned primarily to the battery (for energy support) while the high-frequency component is assigned to the supercapacitor (for transient power). The HESS current can be expressed by:

$$i_{HESS} = i_b + i_{sc} = \frac{v_{bdc1}}{v_{dc}} i_{b0} + \frac{v_{bdc2}}{v_{dc}} i_{sc0} \quad (14)$$

Furthermore, based on Fig. 1, the dynamics that represents power follow at the DC microgrid bus can be formulated as follows:

$$C_{dc} v_{dc} \frac{dv_{dc}}{dt} = P_{Cdc} = P_{dc} - P_L \quad (15)$$

where P_{dc} represent the DC microgrid power (W), P_L is the power of load (W), and P_{dc} is the integrated PV/battery/supercapacitor power (W), which is given by:

$$P_{dc} = v_{dc} i_{pv} + v_{dc} i_b + v_{dc} i_{sc} \quad (16)$$

where $P_{pv} = v_{dc} i_{pv}$ is the PV/BC system output power, $P_b = v_{dc} i_b$ is battery/BDDC system output power, and $P_{sc} = v_{dc} i_{sc}$ is the supercapacitor/BDDC system output power.

Control system design

This section provides a comprehensive analysis of the control strategies developed for the proposed energy management system approach. It initially presents the proposed control methodology for the integrated energy management system, highlighting the coordination of multiple energy sources to enhance system stability and operational efficiency. Subsequently, we investigate the specific control techniques employed within the photovoltaic subsystem, including maximum power point tracking algorithm and the associated control mechanisms that are responsive to fluctuating environmental conditions. The control methodologies outlined herein form the foundation of the system's capability to effectively harvest, store, and distribute renewable energy while maintaining reliability across a range of operational scenarios.

Proposed control approach for energy management system

The suggested control structure consists of a DC microgrid bus voltage control loop featuring a PI controller and a state observer that employs a non-linear high-gain observer. Subsequently, the output obtained from the PI-NHGO loop is split by a low-pass filter into two parts. Next, the reference currents obtained for both the battery and supercapacitor are compared with the measured currents. The difference is then sent to the PI controllers to ensure proper regulation of battery and supercapacitor currents. The proposed control scheme is illustrated in Fig. 8.

Design of the outer control layer

The voltage regulation loop is the external supervision layer of the proposed control strategy. The function of this layer is to guarantee that the DC microgrid bus voltage remains at its specified nominal level, regardless of fluctuations in the load and variations in the production of renewable energy sources. This section elaborates on the design methodology for the outer control layer.

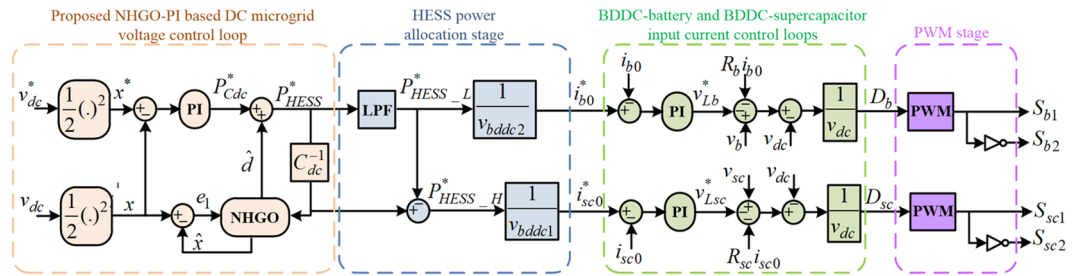


Fig. 8. Schematic diagram of the proposed control structure for the HESS-based DC microgrid.

Non-linear high gain observer design

The variation in the power caused by PV and resistive load leads to fluctuations in the voltage, and a state observer is designed to compensate for its influence. In this work, the observer has been integrated into the microgrid voltage control loop within the overall control circuit of the DC-microgrid based HESS. Since the variation in PV and resistive power provides harmful power pulses to the microgrid, their power can be considered as an external disturbance. Given this condition, and by substituting Eqs.(14), (15), and (16) into the DC microgrid bus voltage dynamics in Eq.(13), we have:

$$C_{dc}v_{dc} \frac{dv_{dc}}{dt} = P_{pv} + P_{HESS} - P_L \tag{17}$$

where P_{HESS} is the HESS output power, which is expressed by:

$$P_{HESS} = i_{HESS}v_{dc} = (i_b + i_{sc})v_{dc} \tag{18}$$

To design the proposed NHGO according to^{36,37,43}, we define the $x = \frac{v_{dc}^2}{2}$ as first state, $u_c = P_{HESS} = v_{dc}(i_b + i_{sc})$ as the controller output, and $d = \frac{P_{pv} - P_L}{C_{dc}}$ is the second state representing the disturbances that affecting the DC microgrid bus system. Hence, the d term's changes as a function of the variations in load demand and PV output power.

Before proceeding with the observer design, we establish the following assumptions that form the mathematical foundation for the NHGO development and its stability guarantees:

Assumption 1 The half-square DC microgrid bus voltage $x = \frac{v_{dc}^2}{2}$ and its derivative \dot{x} are bounded in the operating region, $\|x\| \leq M_1$, $\|\dot{x}\| \leq M_2$, where $M_1, M_2 > 0$ are known constants determined by physical voltage limits and circuit dynamics. This assumption is inherently satisfied in practical DC microgrids due to protection limits and converter saturation.

Assumption 2 The disturbance $d(t)$, representing load variations and PV power fluctuations is bounded, $|d(t)| \leq d_{max}, \forall t \geq 0$. This is physically justified since both load power and PV generation have finite maximum values constrained by system capacity.

Assumption 3 The saturation function used in the NHGO design defined in (to be defined in Eq. 93) is globally Lipschitz continuous with constant $L_{sat} = \frac{1}{f}$. This property ensures bounded observer gains during large estimation errors and enables smooth transition between dynamic and steady-state regimes.

Assumption 4 The observer gains are chosen sufficiently large compared to PI controller parameters, $\beta_1 \gg K_{pv}$ and $\beta_2 \gg K_{iv}$. This ensures time-scale separation between fast observer dynamics (rapid disturbance estimation) and slower controller dynamics (voltage regulation), preventing interference between the two control layers.

Assumption 5 The initial estimation errors are bounded, $\|e_1(0)\| = \|x(0) - \hat{x}(0)\| \leq \rho_0$, where ρ_0 is a finite positive constant. This assumption is practical since initial estimates can be set based on nominal operating conditions or previous system states.

Under these assumptions, the NHGO provides exponential convergence of estimation errors to a bounded zone near zero, with the ultimate bound determined by the disturbance magnitude d_{max} and measurement noise level η_{max} . The complete closed-loop stability proof using Piecewise Quadratic Lyapunov Functions (PQLF) is provided in the Appendix, demonstrating that the proposed NHGO achieves asymptotic stability in both dynamic (high-gain) and steady-state (low-gain) operating regimes. The design process of the proposed NHGO is begins with the classical ESO, which is widely used in disturbance-estimation methods. The ESO augments the perturbed system's in Eq.(11) by introducing an additional "extended" state that represents the total lumped

disturbance acting on the plant. Considering Eq.(17), the augmented perturbed model can be written as state-space model as given in Eq.(19):

$$\begin{bmatrix} \dot{x} \\ \dot{d} \end{bmatrix} = \begin{bmatrix} 0 & 1 \\ 0 & 0 \end{bmatrix} \begin{bmatrix} x \\ d \end{bmatrix} + \begin{bmatrix} \frac{1}{C_{dc}} \\ 0 \end{bmatrix} u_c + \begin{bmatrix} 0 \\ 1 \end{bmatrix} h(t) \tag{19}$$

where $h(t)$ is the time derivative of d , which is given by:

$$\dot{d} = h(t) = \frac{1}{C_{dc}} \left(\frac{d}{dt} P_{pv} - \frac{d}{dt} P_L \right) \tag{20}$$

It is important to notice that in real-life conditions, disturbances vary frequently. Hence, x , d and $h(t)$ are bounded, $|d(t)| \leq D_{max}$, $|h(t)| \leq H_{max} \forall t \geq 0$ (consistent with Assumption 2), and $h(t)$ is locally Lipschitz^{18,37}. The local Lipschitz property of $h(t)$ ensures that the disturbance derivative does not exhibit infinite rate of change, which is physically justified since PV power and load variations have finite slew rates determined by physical constraints.

Let's define e_1 as the observer error and e_2 as the disturbance estimation error, with $e_1 = y_m - \hat{x}$ and $e_2 = d - \hat{d}$. In this \hat{x} represent the estimated state of x , and \hat{d} is the estimated state of d , and y_m represent the measured output (DC microgrid bus voltage), which is given by:

$$y_m(t) = y(t) + n(t) = x(t) + \eta(t) \tag{21}$$

where $y = x$ represents the system output variable (the half-square DC microgrid bus voltage) and $\eta(t)$ is the measurement noise, which is assumed to be bounded, $|\eta(t)| \leq \eta_{max}$ (consistent with practical sensor noise characteristics). This bounded noise assumption, combined with the variable-gain mechanism of the NHGO, enables superior noise immunity in steady-state operation compared to other observers.

The respective ESO is expressed by Eq.(22).

$$\begin{cases} \dot{\hat{x}} = \frac{1}{C_{dc}} u_c + \hat{d} + \beta_1 e_1 \\ \dot{\hat{d}} = \beta_2 e_1 \end{cases} \tag{22}$$

where β_1 and β_2 are the ESO gains, determined through the pole allocation approach according to³⁰, which are given by $\beta_1 = 2\omega_{eso}$, $\beta_2 = \omega_{eso}^2$. ω_{eso} is the bandwidth of the ESO and is selected in accordance to the natural frequency of the voltage regulator^{44,45}. This configuration allows simultaneous estimation of the system state and corresponding disturbance, thus improving disturbance rejection capability and robustness without requiring an accurate model.

Although the ESO provides reliable disturbance estimation, its performance depends heavily on the gain selection. Increasing the ESO gains enhances estimation speed but also amplifies measurement noise in e_1 . Consequently, a trade-off exists between fast disturbance tracking and noise immunity. In applications such as DC microgrids, where the system is subject to abrupt irradiance or load variations, this compromise limits ESO effectiveness. To overcome the slow disturbance-tracking behavior of the ESO while maintaining a simple structure, another observer is proposed, named the HGO³⁵, which accelerates disturbance estimation by scaling the first ESO gain β_1 with a small positive parameter k_1 and the second ESO gain β_2 with the squared of this parameter (k_1^2), as given in Eq.(23).

$$\begin{cases} \dot{\hat{x}} = \frac{1}{C_{dc}} u_c + \hat{d} + \frac{\beta_1}{k_1} e_1 \\ \dot{\hat{d}} = \frac{\beta_2}{k_1^2} e_1 \end{cases} \tag{23}$$

with $0 < k_1 \ll 1$. By decreasing k_1 , the observer poles move far left in the complex plane, yielding rapid convergence of \hat{x} and \hat{d} to their true values.

This structure substantially improves transient disturbance rejection because the estimated disturbance reacts quickly to dynamic changes.

Despite its improved disturbance estimation speed, the HGO inherits a critical drawback: measurement-noise amplification. The observer error e_1 is multiplied by large factors $\frac{\beta_1}{k_1}$ and $\frac{\beta_2}{k_1^2}$; thus, even small sensor noise produces large oscillations in the estimated states and, consequently, in the control input. Reducing k_1 further intensifies this effect, while increasing it sacrifices estimation speed. Therefore, researchers sought an observer capable of adapting its gain dynamically using high gain during transients for rapid disturbance estimation and lower gain during steady state to attenuate measurement noise. This requirement motivated the development of the Nonlinear High-Gain Observer (NHGO).

Before developing the proposed NHGO, it is necessary to reformulate the linear correction terms of the traditional HGO into nonlinear ones, following Proposition 1 of⁴⁶. In the standard HGO structure, both correction terms $\frac{\beta_1}{k_1} e_1$ and $\frac{\beta_2}{k_1^2} e_1$ are linear with respect to the observer error e_1 , scaled by constant high-gain factors $\frac{\beta_1}{k_1}$ and $\frac{\beta_2}{k_1^2}$. These linear correction terms ensure rapid convergence but also make the observer extremely sensitive to measurement noise, since any fluctuation in the measured voltage is directly amplified by the high gains. According to the approach proposed in⁴⁶, this drawback can be mitigated by replacing the linear

correction terms with nonlinear and bounded functions that preserve the sign of the estimation error while limiting its magnitude. Mathematically, this transformation replaces the linear terms $\frac{\beta_1}{k_1}e_1$ and $\frac{\beta_2}{k_1^2}e_1$ in Eq.(23) by new nonlinear expressions using the *sat* function according to the Proposition 1 in⁴⁶ as given in Eq.(24):

$$\begin{cases} \frac{\beta_1}{k_1}e_1 \text{ becomes } \frac{\beta_1}{k_1}e_1 + \frac{\beta_1 f(k_1 - k_2)}{k_1 k_2} \text{sat} \left(\frac{e_1}{f} \right) \\ \frac{\beta_2}{k_1^2}e_1 \text{ becomes } \frac{\beta_2}{k_1^2}e_1 + \frac{\beta_2 f(k_1^2 - k_2^2)}{k_1^2 k_2^2} \text{sat} \left(\frac{e_1}{f} \right) \end{cases} \quad (24)$$

where $f > \epsilon$ defines the boundary layer of parameters k_1 and k_2 . ϵ defines the lower boundary layer of the observer estimation error ($\epsilon \geq e_1$). The parameter f determines the width of the transition region between the linear (steady-state, low-gain) and saturated (dynamic, high-gain) observer behaviors. A larger f results in a wider boundary layer with smoother gain transitions but slower disturbance response, while a smaller f provides sharper transitions and faster dynamics but may be more sensitive to noise. f should be selected based on the expected amplitude of the estimation error e_1 during transients, which is selected equal 190 in this work.

As shown in Eq.(23), both correction nonlinear terms are represented as the sum of a linear correction terms with a saturation function “*sat*”. The *sat* (.) is introduced into the observer structure to smoothly limit the amplitude of the correction term that depends on the error signal e_1 . Its main purpose is to balance the trade-off between fast disturbance estimation and noise immunity, enabling the observer to behave differently during transient and steady-state conditions.

In the HGO, the observer error e_1 is multiplied by very large constant gains (e.g., $\frac{\beta_1}{k_1}$ and $\frac{\beta_2}{k_1^2}$). When measurement noise is present, even small fluctuations in y can cause large oscillations in the correction terms, destabilizing the observer or injecting noise into the control input. The *sat* (.) function limits the magnitude of this correction, effectively capping the observer’s response when the observer error e_1 exceeds a defined threshold (the boundary layer width, f). This prevents noise or abrupt disturbances from causing excessive observer output. The *sat* (.) is expressed by^{37,43}:

$$\text{sat} \left(\frac{e_1}{f} \right) = \begin{cases} \frac{e_1}{f}; & \text{if } \left| \frac{e_1}{f} \right| \leq D \\ \text{sign} \left(\frac{e_1}{f} \right); & \text{if } \left| \frac{e_1}{f} \right| > D \end{cases} \quad (25)$$

where $D > 0$ is a normalization constant that defines the width of the linear region of the *sat* $\left(\frac{e_1}{f} \right)$. It specifies the range of the argument $\frac{e_1}{f}$ within which the function behaves linearly (i.e., $\text{sat} \left(\frac{e_1}{f} \right) = D \frac{e_1}{f}$) and beyond which it saturates to the fixed limits ± 1 . In this work we use $D = 1$.

The saturation function definition in Eq.(25) is additionally explicitly shows how f determines the switching boundary:

The new nonlinear correction terms in Eq.(22) introduces a variable-gain mechanism governed by a nonlinear saturation (or boundary-layer) function. According to these, the NHGO model is given by the following expression:

$$\begin{cases} \hat{x} = \frac{1}{C_{dc}} u_c + \hat{d} + \frac{\beta_1}{k_1} e_1 + \frac{\beta_1 f(k_1 - k_2)}{k_1 k_2} \text{sat} \left(\frac{e_1}{f} \right) \\ \hat{d} = \frac{\beta_2}{k_1^2} e_1 + \frac{\beta_2 f(k_1^2 - k_2^2)}{k_1^2 k_2^2} \text{sat} \left(\frac{e_1}{f} \right) \end{cases} \quad (26)$$

where β_1 , β_2 , k_1 and k_2 are the proposed NHGO’s gain parameters. In this, to achieve the idea of separate gains using the proposed NHGO, $k_2 \geq 10k_1$ must be satisfied, in which k_1 is adopted when the NHGO operating in dynamic state while k_2 is adopted when the NHGO operating in steady state^{37,43}.

As shown in Eq.(25), the *sat* $\left(\frac{e_1}{f} \right)$ divides the proposed NHGO operation into two regimes, dynamic (transient) regime and steady-state regime, as follows:

Dynamic regime: when $\left| \frac{e_1}{f} \right| > D$, the observer error is large and the *sat* $\left(\frac{e_1}{f} \right)$ is reaches its limit, and the observer behaves like a high-gain system with small parameter k_1 . This allows rapid error convergence and fast disturbance estimation. In this case, the proposed NHGO in Eq.(25) becomes as a HGO as given by Eq.(27):

$$\begin{cases} \hat{x} = \frac{1}{C_{dc}} u_c + \hat{d} - \frac{\beta_1}{k_1} e_1 \\ \hat{d} = \frac{\beta_2}{k_1^2} e_1 \end{cases} \quad (27)$$

Steady-state regime: when $\left| \frac{e_1}{f} \right| \leq D$, the observer error is small and the *sat* $\left(\frac{e_1}{f} \right)$ behaves linearly ($\text{sat} \left(\frac{e_1}{f} \right) = \frac{e_1}{f}$), effectively reducing the observer gain to a low-gain mode with large parameter k_2 , thus attenuating measurement noise and improving steady-state accuracy. In this case, the proposed NHGO in Eq.(24) becomes as given by Eq.(28):

$$\begin{cases} \hat{x} = \frac{1}{C_{dc}} u_c + \hat{d} + \frac{\beta_1}{k_1} e_1 \pm \left[\frac{\beta_1 f(k_1 - k_2)}{k_1 k_2} \right] \\ \hat{d} = \frac{\beta_2}{k_1^2} e_1 \pm \left[\frac{\beta_2 f(k_1^2 - k_2^2)}{k_1^2 k_2^2} \right] \end{cases} \quad (28)$$

Based on Eqs. (27) and (28), it is evident that the proposed NHGO effectively distinguishes between dynamic and steady-state operating regimes, thereby balancing disturbance-rejection dynamics and noise immunity. During transient regime, a smaller parameters k_1 is employed to enable rapid disturbance estimation and rejection without compromising steady-state accuracy. Conversely, in the steady-state regime, a larger parameters k_2 is utilized to suppress measurement noise and minimize estimation errors while maintaining satisfactory transient disturbance-rejection performance. The overall diagram of the suggested NHGO is illustrated in Fig. 9.

According to Fig. 9, the estimated disturbance \hat{d} is used to provide feedforward to the output of the microgrid bus voltage regulator I_c^* , compensating for the disturbance while also producing the HESS power reference P^* as in Fig. 8.

Unlike traditional ESO or HGO, the proposed NHGO introduces a nonlinear gain adaptation based on a saturation function that enables automatic transition between high- and low-gain modes. This structure achieves rapid disturbance estimation in transients while maintaining strong noise immunity at steady state. The proposed NHGO retains the same second-order structure as a conventional HGO; it only replaces the linear correction terms with bounded nonlinear functions (as described in Eq. (27)). Hence, its implementation complexity remains comparable to the standard HGO, and it does not require additional differentiators or sliding surfaces, as in the STO and HOSMO approaches. This makes it computationally efficient and well-suited for real-time implementation on embedded platforms like OP5700. Additionally, compared with ESO or STO-based methods that involve multiple gains or require solving Riccati-type equations, the NHGO is tuned with a few intuitive parameters: two gain coefficients (β_1, β_2), two scaling constants (k_1, k_2), and a boundary-layer width f . This structure makes tuning straightforward and physically interpretable, unlike the complex multi-parameter adjustments needed for HOSMO or improved fuzzy ESO designs.

On the other hand, the proposed NHGO explicitly resolves the long-standing trade-off between disturbance-rejection speed and noise sensitivity observed in conventional observers. The classical ESO provides good robustness but suffers from limited bandwidth, which leads to slow disturbance estimation. The HGO improves estimation speed; however, it significantly amplifies measurement noise due to its constant high gain. Advanced observers such as the STO and HOSMO offer improved robustness, but they introduce higher-order dynamics, chattering effects, and complex tuning procedures that increase implementation difficulty. In contrast, the proposed NHGO achieves an effective balance between these conflicting objectives by employing a nonlinear, adaptive gain mechanism. This design enables the observer to operate with a high gain during transients for fast disturbance estimation and a reduced gain in steady state to suppress noise amplification and minimize estimation error.

DC microgrid bus voltage PI controller design

In a PV/battery/supercapacitor-based DC microgrid supplying DC loads, maintaining the voltage plays a vital role in maintaining the overall stability, power balance, and reliability of the system. The DC microgrid bus voltage serves as a common link that reflects the instantaneous balance between generated power, stored energy, and load demand. When generation exceeds the load demand, the DC microgrid bus voltage tends to rise, whereas a deficit in generation causes it to drop. The voltage regulation mechanism detects these variations and coordinates the operation of the HESS to restore the voltage to its reference. In this coordination, the battery provides slow, high-energy compensation for long-term power unbalances, while the supercapacitor delivers fast, high-power support to mitigate transient fluctuations. Additionally, the DC microgrid bus voltage regulation compensates for disturbances caused by variations in PV generation and load demand, ensuring smooth energy flow, stable converter operation, and high-quality power delivery to the DC loads, thus ensuring

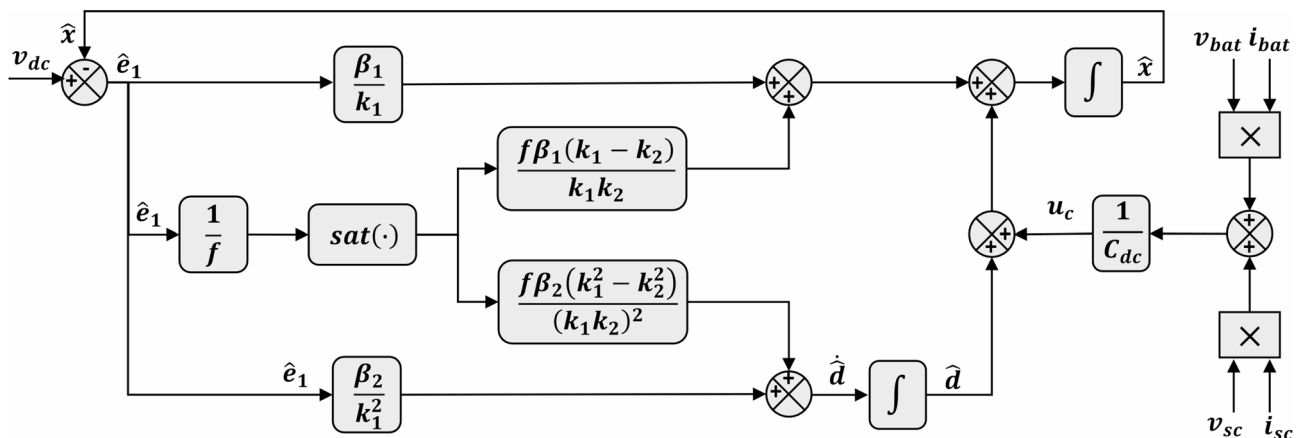


Fig. 9. Schematic diagram of the proposed NHGO.

the system operates reliably and consistently. So, in this section we present the control of the microgrid bus voltage using the PI to provide the reference currents of both inner control loops (the inner BDDC-based battery input current control loop and the inner BDDC-based supercapacitor input current control loop). The diagram of the closed-loop DC microgrid voltage regulation is shown in Fig. 10.

According to Eq.(17), the DC microgrid bus capacitor reference power P_{Cdc}^* , the PV output power P_{pv} , and the load power P_{load} are used to determine the HESS reference power P_{HESS}^* . This reference power is extracted using a first order Low-Pass Filter (LPF) with cut-off frequency of $f_c = 20$ kHz to obtain the output reference currents for both the BDDC-based battery system (i_b^*) and the BDDC-based supercapacitor system (i_{sc}^*). These reference currents are then used to determine the inner BDDC-based battery input current control loop (i_{b0}^*) and the inner BDDC-based supercapacitor input current control loop (i_{sc0}^*), based on the relationship between the BDDC input and output currents given in Eq.(12).

According to Fig. 1, P_{Cdc}^* is generated from the regulation of the half-square DC microgrid bus voltage ($x = \frac{v_{dc}^2}{2}$) with its reference ($\frac{v_{dc}^{2*}}{2}$) using a PI controller as follows:

$$P_{Cdc}^* = \left(K_{pv} + \frac{K_{iv}}{s} \right) \left(\frac{v_{dc}^{2*}}{2} - \frac{v_{dc}^2}{2} \right) \tag{29}$$

From Eqs.(15), (17), and (18), we have:

$$C_{dc}v_{dc} \frac{dv_{dc}}{dt} = P_{dc} = P_{HESS} - \hat{d}C_{dc} \tag{30}$$

Based on Eqs. (29) and (30), we obtained P_{HESS}^* as follows:

$$P_{HESS}^* = \left(K_{pv} + \frac{K_{iv}}{s} \right) \left(\frac{v_{dc}^{2*}}{2} - \frac{v_{dc}^2}{2} \right) + \hat{d}C_{dc} \tag{31}$$

where K_{pv} and K_{iv} are the DC microgrid bus voltage PI parameters, determined through the pole allocation approach as in the following equation:

$$\begin{cases} K_{pv} = 2\xi_v \omega_{nv} C_{dc} \\ K_{iv} = C_{dc} \omega_{nv}^2 \end{cases} \tag{32}$$

where ω_{nv} denotes the natural frequency of the PI controller and ξ_v its damping ratio. ω_{nv} is selected to provide good separation between the natural frequency of the DC microgrid voltage control loop and the natural frequency of the BDDC-battery and BDDC-supercapacitor input current control loops according to the cascade PI parameters tuning methodology in⁴⁴.

Figure 11 illustrates the step response of the DC microgrid bus system. According to this figure, it can be seen that the increase of the PI gain values results in a leftward shift of the poles, thereby speeding the system through a broader bandwidth and enhancing tracking at low frequencies. Nonetheless, this increase in gain can lead to considerable overshoot and a decrease in phase margin, thereby heightening the system's sensitivity to noise and variations in parameters. Lower gain settings result in slower but more robust performance, whereas higher gain settings offer faster responses but may be prone to instability. Typically, optimal gain values are selected to strike an effective balance among speed, accuracy, and robustness.

Design of the inner control layer

The internal control loop is the basis of the multi-layer control strategy. It ensures rapid control and monitoring of the HESS current while protecting the associated devices. This control layer enables the external supervision loop to reliably achieve the objectives at the system level. This section elaborates on the design methodology for the inner control layer.

Supercapacitor current control loop

In this section, the inner current control loop is designed to regulate the BDDC-based supercapacitor system input current i_{sc0} , aiming to improve the BDDC-based supercapacitor system input current quality, protect the BDDC power circuit against overcurrent, and to provide the duty cycle for the BDDC-based supercapacitor system D_{sc} according to the dynamic model of the BDDC-based supercapacitor system input current in Eq.(12) to makes the supercapacitor delivers fast and high-power support to mitigate transient fluctuations. The diagram of the PI in the supercapacitor current control loop is shown in Fig. 12.

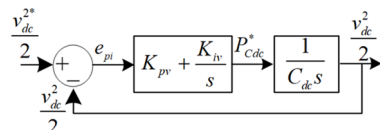


Fig. 10. Diagram of the closed-loop DC microgrid voltage regulation.

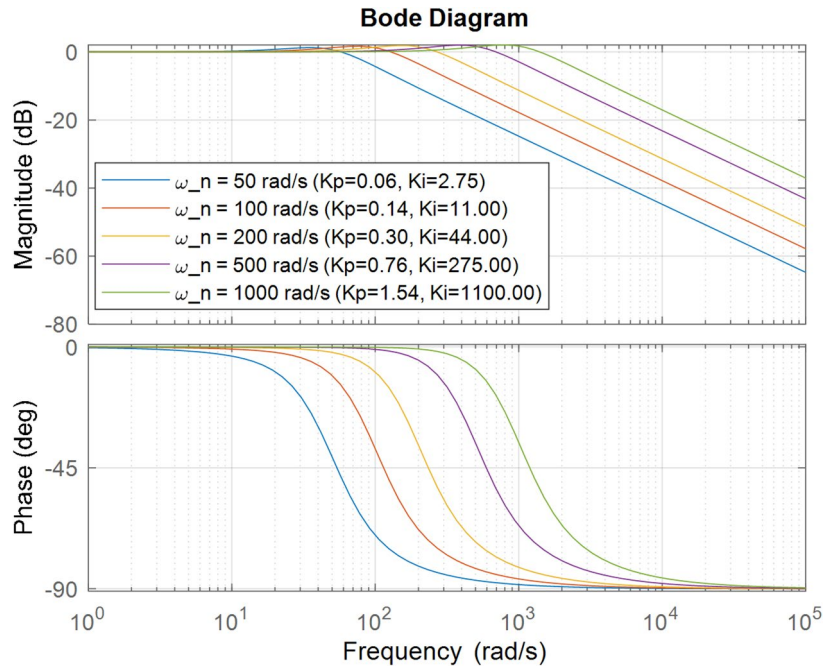


Fig. 11. Frequency response of the DC microgrid bus voltage plant.

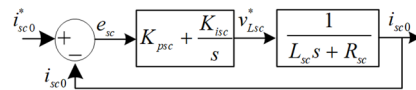


Fig. 12. Closed-loop BDDC-based supercapacitor system current regulation.

As shown in Fig. 12, the output of the PI-based BDDC-based supercapacitor system input current regulation is given by:

$$v_{Lsc}^* = \left(K_{psc} + \frac{K_{isc}}{s} \right) (i_{sc0}^* - i_{sc0}) \tag{33}$$

In this control loop, the BDDC-based supercapacitor system input current reference i_{sc0}^* is determined using relationship between the BDDC input and output currents in Eq.(12) from the filtration of the HESS reference power (P_{HESS}^*) obtained from the regulation of the DC microgrid bus voltage using the LPF with cut-off frequency of $f_c = 20$ kHz as follows:

$$i_{sc0}^* = \frac{P_{HESS_H}^*}{v_{bdc1}} \tag{34}$$

where $P_{HESS_H}^*$ is the high component of P_{HESS}^* obtained using the LPF as shown in Fig. 8.

v_{Lsc}^* represent the droop voltage across the BDDC-based supercapacitor input filter inductance, which is given according to the dynamic model of the BDDC-based supercapacitor system input current in Eq.(12) by:

$$v_{Lsc}^* = v_{sc} - R_{sc}i_{sc0} - v_{dc} - D_{sc}v_{dc} \tag{35}$$

According to Eqs.(33) and (35), the duty cycle for the BDDC-based supercapacitor system D_{sc} is given by:

$$D_{sc} = \frac{1}{v_{dc}} \left(- \left(K_{psc} + \frac{K_{isc}}{s} \right) (i_{sc0}^* - i_{sc0}) + v_{sc} - R_{sc}i_{sc0} - v_{dc} \right) \tag{36}$$

where K_{psc} and K_{isc} are the BDDC-based supercapacitor system input current PI parameters, determined also through the pole allocation approach as in Eq. (37):

$$\begin{cases} K_{psc} = 2\zeta_{sc}L_{sc}\omega_{nsc} - R_{sc} \\ K_{isc} = L_{sc}\omega_{nsc}^2 \end{cases} \tag{37}$$

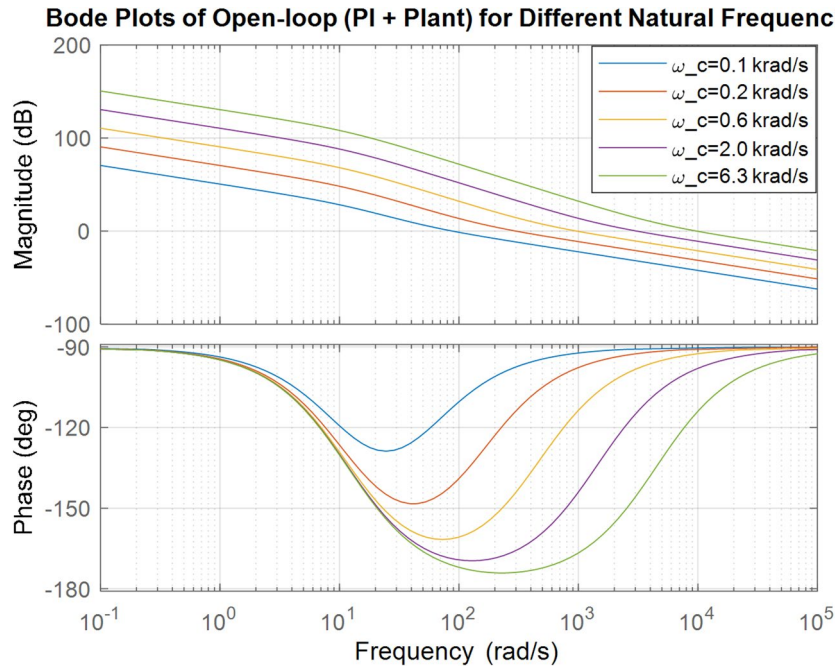


Fig. 13. Frequency response of supercapacitor control system.

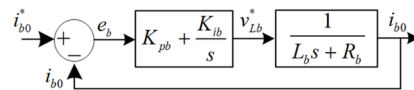


Fig. 14. Closed-loop BDDC-based battery system input current regulation.

where $\omega_{n.sc}$ is the frequency of the BDDC-based supercapacitor system input current PI controller and ζ_{sc} its damping factor.

The Frequency response of supercapacitor current control system under the variation of $\omega_{n.sc}$ is given in Fig. 13. The analysis presented in this figure indicates that the elevation of the natural frequency is attributable to both heightened gains and expanded bandwidth, whereas the phase margin remains relatively stable around 65° thus ensuring robustness. Lower values of $\omega_{n.sc}$ lead to a decreased bandwidth, resulting in a slower response to the supercapacitor’s current. Conversely, elevated values necessitate impractically high gains, rendering the system excessively susceptible to noise and fluctuations. Suitable gains facilitate rapid and adaptable support for the supercapacitor by utilizing gain parameters that are practically attainable.

Battery current control loop

In this section, the inner current control loop is designed to regulate the BDDC-based battery system input current i_{b0} . Its objectives are to improve the input current quality of the BDDC-based battery system, protect the BDDC power circuit from overcurrent conditions, and generate the corresponding duty cycle D_b based on the dynamic model of the BDDC battery input current presented in Eq.(12). This control strategy enables the battery to deliver slow, high-energy compensation for long-term power imbalances. The representation diagram of the PI controller in the battery current control loop is illustrated in Fig. 14.

As shown in Fig. 14, and similar to the BDDC-based supercapacitor system input current regulation discussed in Sect. (3.3.1), the output of the PI-based BDDC battery system input current controller is expressed as:

$$v_{Lb}^* = \left(K_{pb} + \frac{K_{ib}}{s} \right) (i_{b0}^* - i_{b0}) \tag{38}$$

In this control loop, the reference input current of the BDDC-based battery system (i_{b0}^*) is determined based on the relationship between the BDDC input and output currents given in Eq.(12). It is obtained from the low component of HESS reference power ($P_{HESS_L}^*$), which is derived from the filtration of P_{HESS}^* using the LPF, as follows:

$$i_{b0}^* = \frac{P_{HESS_L}^*}{v_{bdc2}} \tag{39}$$

where $P_{HESS_L}^*$ is the low component of P_{HESS}^* obtained using the LPF as shown in Fig. 8.

v_{Lb}^* represent the droop voltage across the BDDC-based battery input filter inductance, which is given according to the dynamic model of the BDDC-based battery system input current in Eq.(12) by:

$$v_{Lb}^* = v_b - R_b i_{b0} - v_{dc} - D_b v_{dc} \tag{40}$$

According to Eqs.(38) and (40), the duty cycle for the BDDC-based supercapacitor system D_{sc} is given by:

$$D_b = \frac{1}{v_{dc}} \left(- \left(K_{pb} + \frac{K_{ib}}{s} \right) (i_{b0}^* - i_{b0}) + v_b - R_b i_{b0} - v_{dc} \right) \tag{41}$$

where K_{pb} and K_{ib} are the BDDC-based battery system input current PI parameters, determined also using pole allocation approach as in Eq. (42):

$$\begin{cases} K_{pb} = 2\zeta_b L_b \omega_{nb} - R_b \\ K_{ib} = L_b \omega_{nb}^2 \end{cases} \tag{42}$$

where ω_{nb} is the natural frequency of the BDDC-based battery system input current PI controller and ζ_b its damping factor.

In this work, both ω_{nsc} and ω_{nb} are selected in accordance to their corresponding switching frequency of the BDDC to provide good dynamic responses and ripple attenuations separation based on the PI parameters tuning methodology in⁴⁴.

Photovoltaic system control

A nonlinear MPPT approach was adopted in this investigation to obtain an optimal operating point that maximizes the output power of the PV panel. An integral backstepping (IBSC) controller is used instead of the cascaded-loop PI controllers to improve the accuracy of MPP tracking. The reference voltage supplied to the IBSC controller is acquired using the classical INC algorithm. The control strategy implemented for the PV-side system is shown in Fig. 15.

The PV system serves as the primary renewable energy source in the proposed DC microgrid. To maximize energy harvesting under varying environmental conditions (irradiance and temperature fluctuations), the PV system requires: (i) accurate MPPT to determine the optimal operating voltage, and (ii) robust voltage regulation control to maintain the PV output at the identified MPP despite system disturbances. This section presents the integrated control strategy for the PV-side system, combining the Incremental Conductance (InC) MPPT algorithm with an Integral Backstepping Controller (IBSC) for superior tracking performance and disturbance rejection. The PV control system comprises two cascaded layers, as illustrated in Fig. 15:

1. Reference Generation Layer (Sect. 4.1): The InC-MPPT algorithm processes measured PV voltage and current to compute the optimal reference voltage v_{pv}^* that corresponds to the MPP under current environmental conditions.
2. Tracking Control Layer (Sect. 4.2): The IBSC controller regulates the boost converter duty cycle D_{pv} to force the actual PV voltage v_{pv} to accurately track the reference v_{pv}^* , ensuring operation at the MPP while rejecting disturbances from DC bus voltage variations and rapid irradiance changes.

This two-layer architecture decouples MPPT decision-making from converter control execution, enabling independent tuning and robust performance under diverse operating scenarios.

The PV system control is developed in two stages, as follows:

PV reference voltage generation

The InC is an online algorithm approach operates by measuring PV voltage v_{pv} and current i_{pv0} at discrete time intervals and computing their incremental changes as follows:

$$\begin{cases} \Delta v_{pv} = v_{pv}(k) - v_{pv}(k-1) \\ \Delta i_{pv} = i_{pv}(k) - i_{pv}(k-1) \end{cases}$$

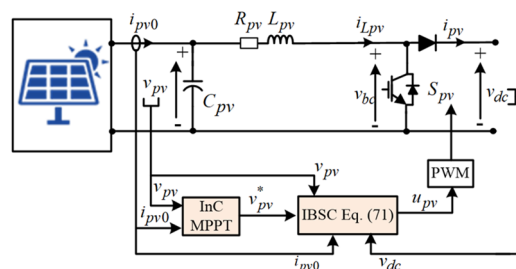


Fig. 15. The implemented control for the boost converter of the PV system.

Based on the comparison between incremental and instantaneous conductance, the reference voltage v_{pv}^* is updated according to the following decision logic:

$$v_{pv}^* = \begin{cases} v_{pv}^* + \Delta v; if \frac{\Delta i_{pv0}}{\Delta v_{pv}} > -\frac{i_{pv0}}{v_{pv}} \\ v_{pv}^* & ; if \frac{\Delta i_{pv0}}{\Delta v_{pv}} = -\frac{i_{pv0}}{v_{pv}} \\ v_{pv}^* - \Delta v; if \frac{\Delta i_{pv0}}{\Delta v_{pv}} < -\frac{i_{pv0}}{v_{pv}} \end{cases} \quad (43)$$

where $v_{pv}^*(k)$ is the reference voltage generated at time step k and Δv is the voltage perturbation step size (typically 0.5–2.5% of v_{mmp}). In this algorithm the sign of $(\frac{\Delta i_{pv0}}{\Delta v_{pv}} = -\frac{i_{pv0}}{v_{pv}})$ indicates the operating point position relative to the MPP.

PV side control design

This section presents the development of an IBSC controller specifically tailored for the PV-side converter to ensure efficient MPPT and enable a smooth energy supply. The primary goal of this approach is to maintain the PV voltage at its reference level, which is set based on the MPPT algorithm, while considering the uncertainties of the system parameters and the impact of environmental changes, including variations in irradiance and temperature. Employing a backstepping approach enables the development of a systematic framework based on Lyapunov theory that guarantees the overall stability of the closed loop system⁴⁷. Meanwhile, incorporating an integral action eliminates steady-state errors and enhances tracking performance, particularly in response to abrupt changes in load demand or weather conditions. The proposed method significantly improves the transient response and disturbance rejection capability compared with traditional methods, making it a more suitable choice for this implementation⁴⁸. The IBSC regulates the instantaneous PV voltage to the reference value provided by the INC-MPPT algorithm, resulting in accurate PV voltage regulation, improved robustness, and enhanced MPP tracking accuracy and PV power production.

To design the Backstepping regulator for the BC-based PV system, the dynamic models of the PV output voltage and BC input current in Eq. (88) are written as state-space model as given in Eq.(44):

$$\begin{bmatrix} \dot{x}_1 \\ \dot{x}_2 \end{bmatrix} = \begin{bmatrix} 0 & -\frac{1}{C_{pv}} \\ \frac{1}{L_{pv}} & \frac{R_{pv}}{L_{pv}} \end{bmatrix} \begin{bmatrix} x_1 \\ x_2 \end{bmatrix} + \begin{bmatrix} \frac{1}{C_{pv}} \\ 0 \end{bmatrix} u_{pv} + \begin{bmatrix} \frac{1}{C_{pv}} & \frac{1}{L_{pv}} \end{bmatrix} \begin{bmatrix} i_{pv0} \\ v_{dc} \end{bmatrix} \quad (44)$$

where x_1 and x_2 denote respectively the voltage v_{pv} and current $i_{L_{pv}}$ states. $u_{pv} = D_{bc}$ represents the duty cycle of the DC DC boost converter-based PV system. i_{pv0} is the PV cell current (Eq. 95), which acts as a disturbance input dependent on environmental conditions.

The IBSC design is typically follows a systematic recursive procedure consisting of three main steps: (i) the definition of the tracking error and introduction of the Integral action, (ii) the definition of the first Lyapunov function and virtual control, and (iii) the definition of the second error surface and final control law.

First, we define the primary tracking error between the PV voltage and its reference e_{bs1} as in Eq. (45).

$$e_{bs1} = x_1 - x_1^* \quad (45)$$

where x_1^* represents the PV voltage reference value (v_{pv}^*).

The derivative of e_{bs1} is given by:

$$\dot{e}_{bs1} = \dot{x}_1 - \dot{x}_1^* = \frac{i_{pv0}}{C_{pv}} - \frac{x_2}{C_{pv}} - \dot{x}_1^* \quad (46)$$

To eliminate steady-state errors and enhance the robustness against uncertainties with improved system performance, the integral action ξ of the error e_{bs1} is introduced as follows:

$$e_{bs} = e_{bs1} + k\xi \quad (47)$$

where $k > 0$ is the integral gain weighting factor, determining the influence of accumulated error on the control action.

$$\xi = \int_0^t e_{bs1} dt \quad (48)$$

To ensure convergence of e_{bs1} and ξ to zero, we construct the first Lyapunov candidate function as follows:

$$V_{bs1} = \frac{1}{2}e_{bs1}^2 + \frac{k}{2}\xi^2 \quad (49)$$

This function is positive definite ($V_{bs1} > 0$ for $e_{bs1} \neq 0$ or $\xi \neq 0$) and radially unbounded.

The derivative of this Lyapunov function is given by:

$$\dot{V}_{bs1} = e_{bs1}\dot{e}_{bs1} + k\xi\dot{\xi} \quad (50)$$

$$\dot{V}_{bs1} = e_{bs1} \left(\frac{i_{pv0}}{C_{pv}} - \frac{x_2}{C_{pv}} - \dot{x}_1^* \right) + k\xi e_{bs1} \quad (51)$$

$$\dot{V}_{bs1} = e_{bs1} \left(\frac{i_{pv0}}{C_{pv}} - \frac{x_2}{C_{pv}} - \dot{x}_1^* + k\xi \right) \quad (52)$$

To ensure controller convergence, the derivative of the Lyapunov function in Eq.(49) must be negative. This yields:

$$\dot{V}_{bs1} = -k_{bs1}C_{pv} \quad (53)$$

where $k_{bs1} > 0$ is the first backstepping gain.

To make \dot{V}_{bs1} negative definite, we choose the virtual control (desired value of x_2) as:

$$x_2 = C_{pv} \left(k_{bs1}e_{bs1} + \frac{i_{pv0}}{C_{pv}} - \dot{x}_1^* + k\xi \right) \quad (54)$$

Let β be the reference of the desired virtual input as follows:

$$\beta = C_{pv} \left(k_1e_{bs1} + \frac{i_{pv0}}{C_{pv}} - \dot{x}_1^* + k\xi \right) \quad (55)$$

The second backstepping error (e_{bs2}) is given now as:

$$e_{bs2} = x_2 - \beta \quad (56)$$

From Eq.(55) we obtain:

$$x_2 = e_{bs2} + \beta \quad (57)$$

Substituting Eq.(57) with its value in Eq.(46), we get:

$$\dot{e}_{bs1} = \frac{i_{pv0}}{C_{pv}} - \frac{e_{bs1} + \beta}{C_{pv}} - \dot{x}_1^* \quad (58)$$

Adding Eq.(55) to Eq.(58):

$$\dot{e}_{bs1} = \frac{i_{pv0}}{C_{pv}} - \frac{e_{bs2} + C_{pv} \left(k_{bs1}e_{bs1} + \frac{i_{pv0}}{C_{pv}} - \dot{x}_1^* + k\xi \right)}{C_{pv}} - \dot{x}_1^* \quad (59)$$

Simplifying Eq. (59) yields:

$$\dot{e}_{bs1} = - \left(\frac{e_{bs2}}{C_{pv}} + k_{bs1}e_{bs1} + k\xi \right) \quad (60)$$

From this, Eq.(50) can be written as follows:

$$\dot{V}_{bs1} = -e_{bs1} \left(\frac{e_{bs2}}{C_{pv}} + k_1e_{bs1} + k\xi \right) + k\xi \dot{\xi} \quad (61)$$

Simplifying Eq.(61), we have:

$$\dot{V}_{bs1} = - \frac{e_{bs1}e_{bs2}}{C_{pv}} - k_{bs1}e_{bs1}^2 \quad (62)$$

Since x_2 (inductor current) cannot be directly assigned, define a second error tracking the deviation from the virtual control as:

$$\dot{e}_{bs2} = \dot{x}_2 - \dot{\beta} \quad (63)$$

$$\dot{\beta} = C_{pv} \left(k_{bs1}\dot{e}_{bs1} + \frac{i_{pv0}}{C_{pv}} - \dot{x}_1^* + k\xi \right) \quad (64)$$

Replacing Eq.(64) with its value in Eq.(63), we obtain:

$$\dot{e}_{bs2} = \dot{x}_2 - C_{pv} \left(-k_{bs1}^2 e_{bs1} - \frac{k_{bs1} e_{bs2}}{C_{pv}} - k_{bs1} k \xi + \frac{\dot{i}_{pv0}}{C_{pv}} \right) + C_{pv} (\dot{x}_1^* - k e_{bs1}) \quad (65)$$

To ensure that both errors (e_{bs1} and e_{bs2}) converge to zero, a Lyapunov function V_{bs2} is introduced, whose derivative must be strictly negative. The function V_{bs2} is defined as follows:

$$V_{bs2} = V_1 + \frac{1}{2} e_2^2 \quad (66)$$

$$\dot{V}_{bs2} = \dot{V}_{bs1} + \dot{e}_{bs2} e_{bs2} \quad (67)$$

Inserting Eq.(62) into Eq.(67), yields:

$$\dot{V}_{bs2} = -\frac{e_{bs1} e_{bs2}}{C_{pv}} - k_{bs1} e_{bs1}^2 + \dot{e}_{bs2} e_{bs2} = -k_{bs1} e_{bs1}^2 + e_{bs2} (\dot{e}_{bs2} - \frac{e_{bs1}}{C_{pv}}) \quad (68)$$

To guarantee that \dot{V}_2 is negative, we make:

$$\dot{e}_{bs2} - \frac{e_{bs1}}{C_{pv}} = -k_{bs2} e_{bs2} \quad (69)$$

Now, the Lyapunov law may be confirmed by substituting Eq.(69) into (68) as follows:

$$\dot{V}_{bs2} = -k_{bs1} e_{bs1}^2 - k_{bs2} e_{bs2}^2 \quad (70)$$

From here, we can construct the backstepping final control law as follows:

$$u_{pv} = 1 - \frac{L_{pv}}{v_{dc}} \left(k_{bs1} e_{bs1} + k_{bs2} e_{bs2} + k k_{bs1} C_{pv} \xi + k_{bs1}^2 C_{pv} e_{bs1} - C_{pv} k e_{bs1} - \frac{e_{bs1}}{C_{pv}} + C_{pv} \dot{x}_1^* - \dot{i}_{pv0} + \frac{x_1}{L_{pv}} \right) \quad (71)$$

Results and discussion

Simulations

This section evaluates the effectiveness of the proposed control strategy in various scenarios. To this end, and to ensure a thorough and meticulous analysis, the microgrid was subjected to four tests using MATLAB/Simulink. First, the adaptability of the proposed control system to abrupt changes in PV irradiation was assessed. Next, the efficacy of the strategy is analyzed, with particular attention to the effects of temperature fluctuations on the PV cells. The performance of the system was then examined under sudden shifts in the load demand. Finally, the robustness of the proposed methodology is investigated in relation to uncertainties in microgrid parameters and their impact on the overall system performance. The DC microgrid system and associated control parameters are given in Tables 1 and 2:

Performance under step changes in PV irradiance with constant load demand

In this scenario, the adaptability of the proposed control scheme to sudden fluctuations in solar radiation was assessed. As shown in Fig. 16, this assessment was conducted under the assumption of a steady load demand, thereby establishing an environment for evaluating the system's responsiveness.

Figure 17a depicts the power response of the microgrid components with the proposed control scheme under sudden irradiance changes while assuming a constant power load demand of 2.3 kW. Initially, the irradiance was around 900 W/m² until 0.3 s, after which a sudden fall to 400 W/m² was recorded. Subsequently, at 0.6 s, the irradiance increased to 700 W/m² for 0.3 s before decreasing to 300 W/m². As can be seen, the photovoltaic panel operated optimally, precisely tracking the maximum power point (MPP), thereby demonstrating the accuracy and effectiveness of the adopted nonlinear MPPT approach. Meanwhile, the HESS, which comprises a battery and supercapacitor, effectively manages both slow and fast load variations, thereby minimizing the stress on batteries and extending their lifespan. Figure 17b and c, and 17d show respectively the DC microgrid bus voltage, and BDDC-based battery input current, and BDDC-based supercapacitor input current (HESS current waveforms) when the PV temperature is varied while the load remains constant at 2 kW. It can be from these figures, that the proposed NHGO-PI controller maintains excellent voltage stability. The DC microgrid bus voltage settles rapidly at its reference of 400 V, exhibiting a maximum overshoot of only 0.25% (approximately 1 V) and a settling time of approximately 25 ms, as shown in Fig. 17b. The steady-state error is practically zero ($|Ess| < 0.1$ V) once the temperature stabilizes. Additionally, the corresponding BDDC-based battery and BDDC-based supercapacitor input currents indicate smooth coordination: the supercapacitor absorbs the fast transient current spike of approximately 1.2 A ($\pm 4\%$) within 10 ms, while the battery current changes gradually to sustain the new steady operating point. This demonstrates that the NHGO correctly distributes transient and steady-state power, ensuring that temperature-induced PV voltage perturbations do not propagate to the DC microgrid bus. As shown in Fig. 18(a), the battery SOC varies smoothly, whereas Fig. 18(b) depicts the faster dynamics of the supercapacitor.

Parameters		
Boost converter-based PV system	Symbols	Values and units
Open loop voltage	V_{oc}	30.6 V
Short circuit current	I_{sc}	8.6 A
Voltage at MPP	V_{MMP}	24.3 V
Current at MPPT	I_{MMP}	7.82 A
Maximum PV power	P_{pvn}	190 W
Number of parallel strings	N	3
Number of modules in series within string	S	6
Number of cells per module	N_s	50
PV capacitor	C_{pv}	95 μ F
Inductance of BC's input filter	L_{pv}	2 mH
Resistance of BC's input filter	R_{pv}	0.0124 Ω
Switching frequency BC-based PV	f_{sw1}	20 kHz
BDDC-based battery system		
Rated voltage	v_b	204.8 V
Maximum capacity	Q_{bess}	50 Ah
BESS's initial state	l	50%
Cut-off Voltage	v_{bc_of}	153 V
BESS's internalresistance	R_{bess}	0.04096 Ω
BESS fully charged voltage	V_{bfc}	238.3846 V
Inductance of BDDC-based Battery input filter	L_b	2 mH
Resistance of BDDC-based Battery input filter	R_b	0.0124 Ω
Switching frequency of BDDC-based Battery	f_{sw2}	20 kHz
DDBC-based supercapacitor system		
Rated voltage	v_{sc}	48 V
Number of cells	N_{sc}	18
Equivalent DC series resistance	ESR	6 m Ω
Number of series capacitors	S_{sc}	9
Number of parallel capacitors	N_{sc}	1
Maximum capacitance	C_{scmax}	165 F
Initial voltage	v_{sc0}	24 V
Open circuit current	i_{scoc}	10 A
Inductance of BDDC's input filter	L_{sc}	0.85 mH
Resistance of BDDC's input filter	R_{sc}	0.0124 Ω
Switching frequency	f_{sw}	20 kHz
DC microgrid bus		
DC microgrid voltage	v_{dc}	400 V
DC microgrid capacitor	C_{dc}	2200 μ F
Power load	P_L	[1 – 3.6] kW
Simulation		
Sampling time	T_s	6 μ s

Table 1. Parameters of the PV/battery/supercapacitor-based DC microgrid system.

Performance under step changes in temperature with constant load demand

This scenario is shown in Fig. 19, which sought to assess the efficacy of the proposed control strategy, considering the impact of temperature variations in photovoltaic cells on the overall performance of the system while maintaining a constant load demand.

Figure 20a shows the power response of the microgrid components with the suggested control scheme to step temperature change. Initially, the temperature was approximately 35 °C until 0.3s, after which a sudden fall to 15 °C was recorded. Subsequently, at 0.6s, the temperature increased to 25 °C for 0.3s, and then stabilized at 50 °C. Throughout these changes, the PV power maintained a high tracking efficiency with minimal oscillations, thereby demonstrating the greater robustness of the proposed nonlinear MPPT control. The supercapacitor device effectively handled high-frequency power from the microgrid, addressing more than 80% of the transient demands, whereas the battery supplied a smooth steady-state power flow with appropriate temperature evolution.

Figure 20b and c, and 20d show respectively the DC microgrid bus voltage, and BDDC-based battery input current, and BDDC-based supercapacitor input current (HESS current waveforms) when the PV temperature is varied while the load remains constant at 2 kW. It can be from these figures, that the proposed NHGO-PI

Parameters	Symbols	Values and units
Proposed NHGO		
First gain	β_1	80
Second gain	β_2	1600
Dynamic scaling parameter	k_1	0.018
Steady state scaling parameter	k_2	0.235
Boundary-layer	f	190
PI controller for DC microgrid voltage		
Proportional gain	k_{pv}	0.43
Integral gain	k_{iv}	42.0366
PI controller for DDBC-based supercapacitor input current		
Proportional gain	k_{psc}	37.7588
Integral gain	k_{isc}	838,920
PI controller for DDBC-based battery input current		
Proportional gain	k_{pb}	11.9381
Integral gain	k_{ib}	19,739
Cut-off frequency of LPF	f_c	10 kHz
Integral backstepping for DC-based PV		
First backstepping parameter	k_{bs1}	250
Second backstepping parameter	k_{bs2}	2800
Integral gain weighting factor	k	1980

Table 2. Control system parameters.

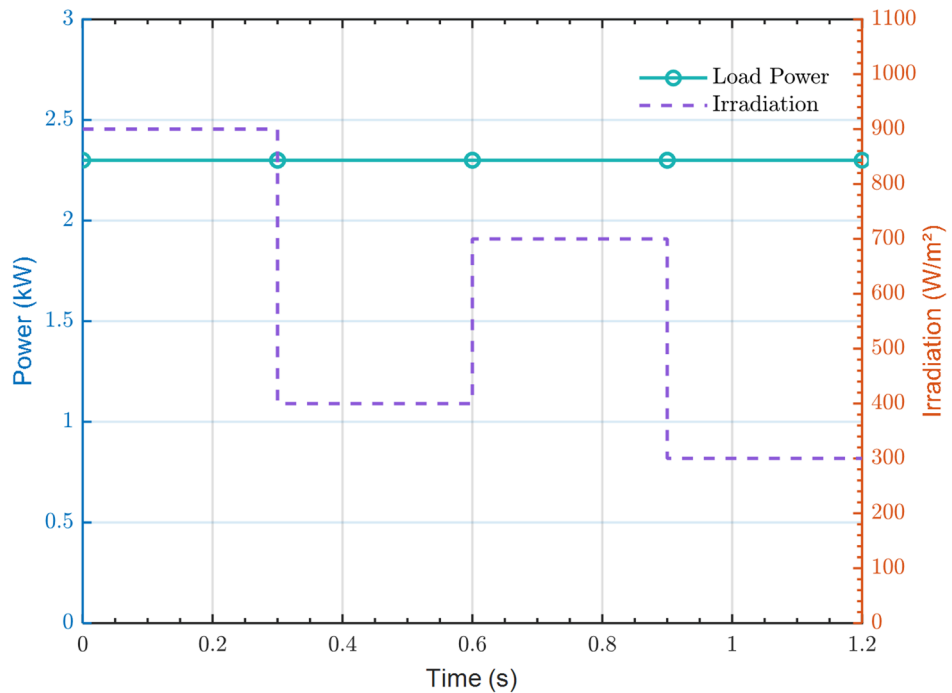


Fig. 16. Test profiles under step changes in irradiance with constant load demand.

controller maintains excellent voltage stability. The DC microgrid bus voltage settles rapidly at its reference of 400 V, exhibiting a maximum overshoot of only 0.25% (approximately 1 V) and a settling time of approximately 25 ms, as shown in Fig. 20b. The steady-state error is practically zero (< 0.1 V) once the temperature stabilizes. Additionally, the corresponding BDDC-based battery and BDDC-based supercapacitor input currents indicate smooth coordination: the supercapacitor absorbs the fast transient current spike of approximately 1.2 A ($\pm 4\%$) within 10 ms (Fig. 20c), while the battery current changes gradually to sustain the new steady operating point, as shown in Fig. 20d. This demonstrates that the NHGO correctly distributes transient and steady-state power, ensuring that temperature-induced PV voltage perturbations do not propagate to the DC microgrid bus.

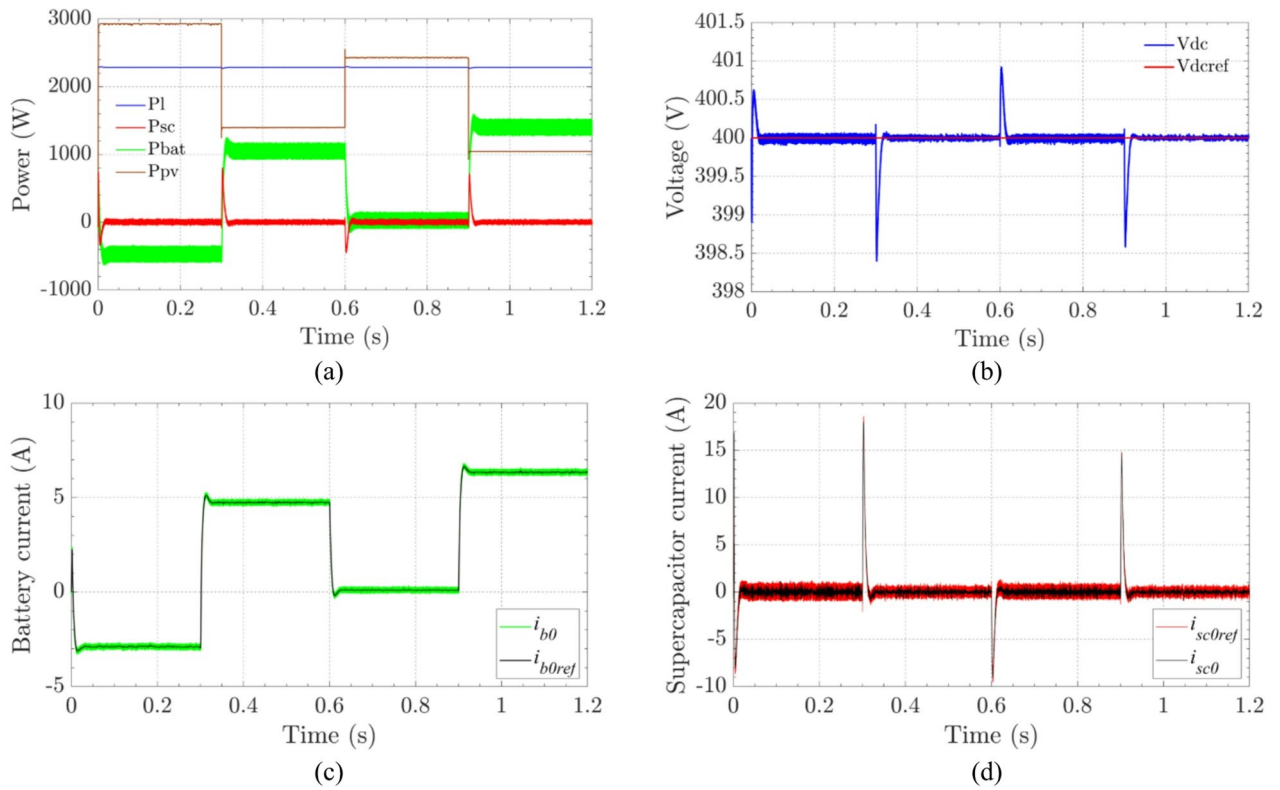


Fig. 17. Simulation results under step change in irradiance (a) different power of the DC microgrid components, (b) DC microgrid bus voltage, (c) BDDC-based battery input current, and (d) BDDC-based supercapacitor input current.

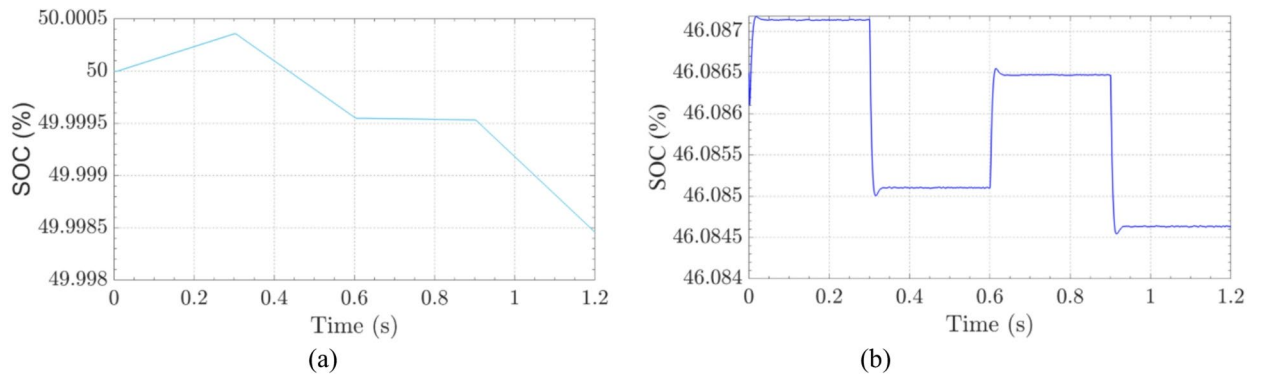


Fig. 18. State of charge (a) Battery, (b) Supercapacitor.

The suggested HESS coordination maintained a good power balance, leading to a faster recovery time and reduced power fluctuations. As illustrated in Fig. 21, the state-of-charge levels of both the batteries and supercapacitor remained within their acceptable operating range. The findings validate the proposed method's ability to sustain the DC microgrid bus voltage level and enhance disturbance rejection while ensuring excellent power allocation, even under variable temperature conditions.

Performance under step change in load demand with constant PV irradiation and temperature

The scenario depicted in Fig. 22 analyzes the system's performance when faced with sudden fluctuations in load demand, all the while keeping solar radiation levels and the photovoltaic panel temperature constant.

Figure 23a illustrates the power response of the microgrid components with the proposed control scheme for fluctuating load demands while assuming a constant solar irradiation of 500 W/m^2 and temperature of 25 C° . Initially, the load demand was approximately 2 kW until 0.3 s, after which a sudden rise in demand to 3.5 kW was recorded. Subsequently, at 0.6 s, the load demand decreased to 1 kW for interval of 0.3 s before increasing

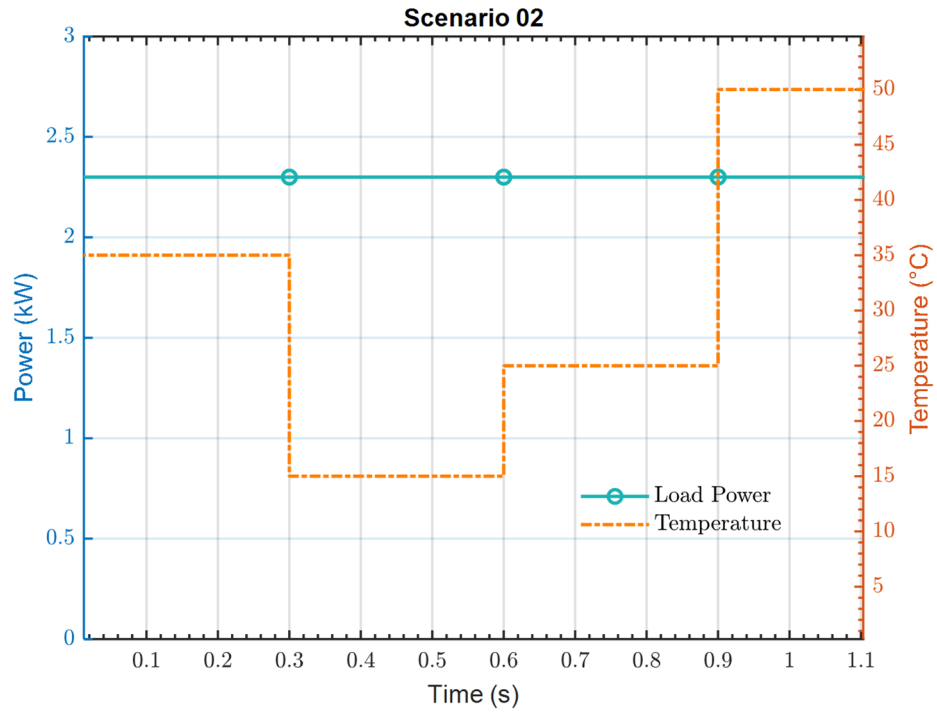


Fig. 19. Test profile under step changes in PV temperature with constant load demand.

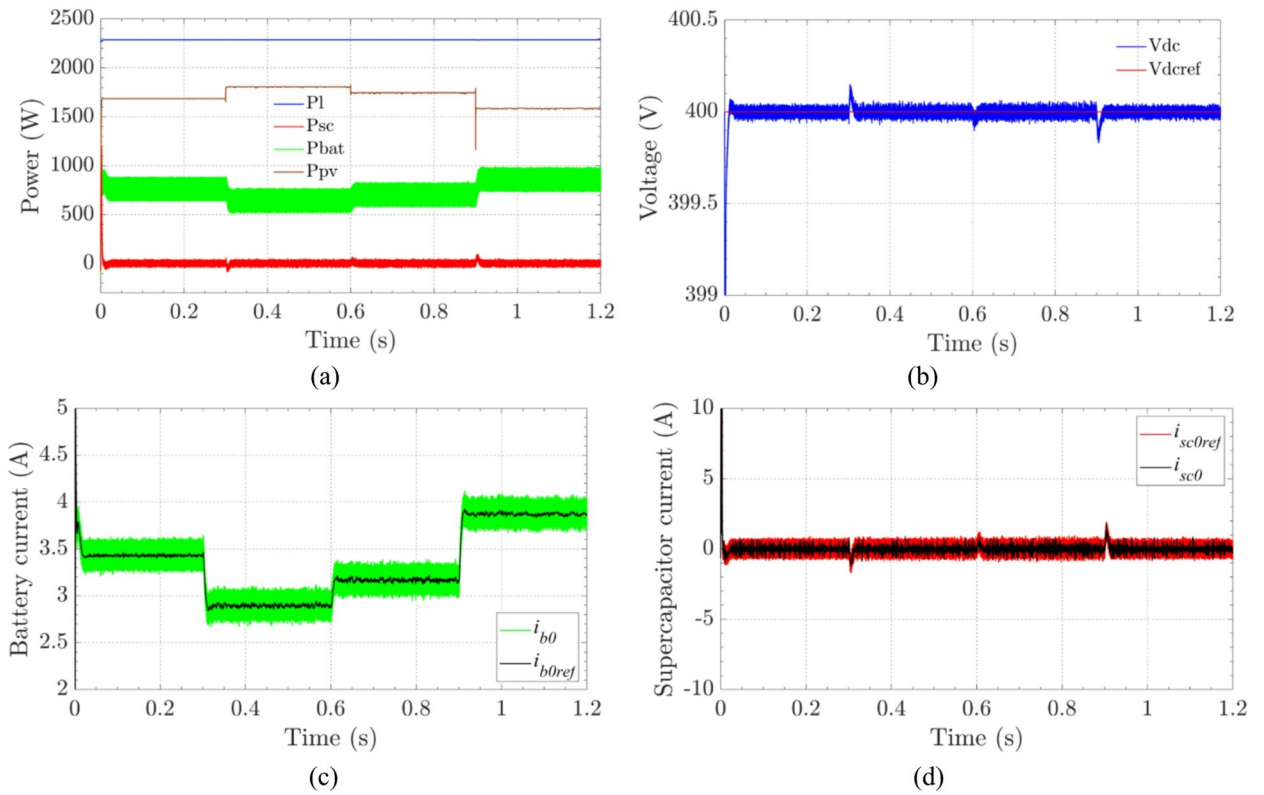


Fig. 20. Simulation results under step changes in PV temperature (a) Different power of the DC microgrid components, (b) DC bus voltage, (c) BDDC-based battery input current, and (d) BDDC-based supercapacitor input current.

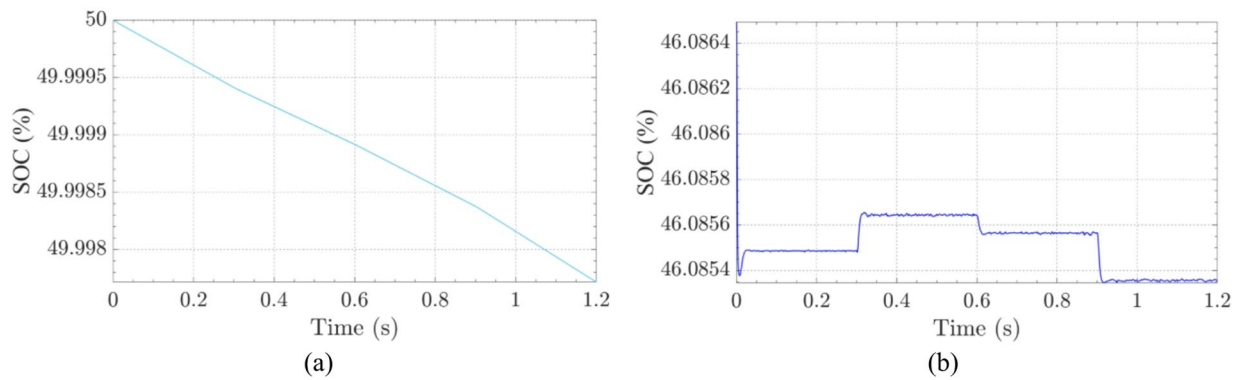


Fig. 21. State of charge (a) Battery. (b) Supercapacitor.

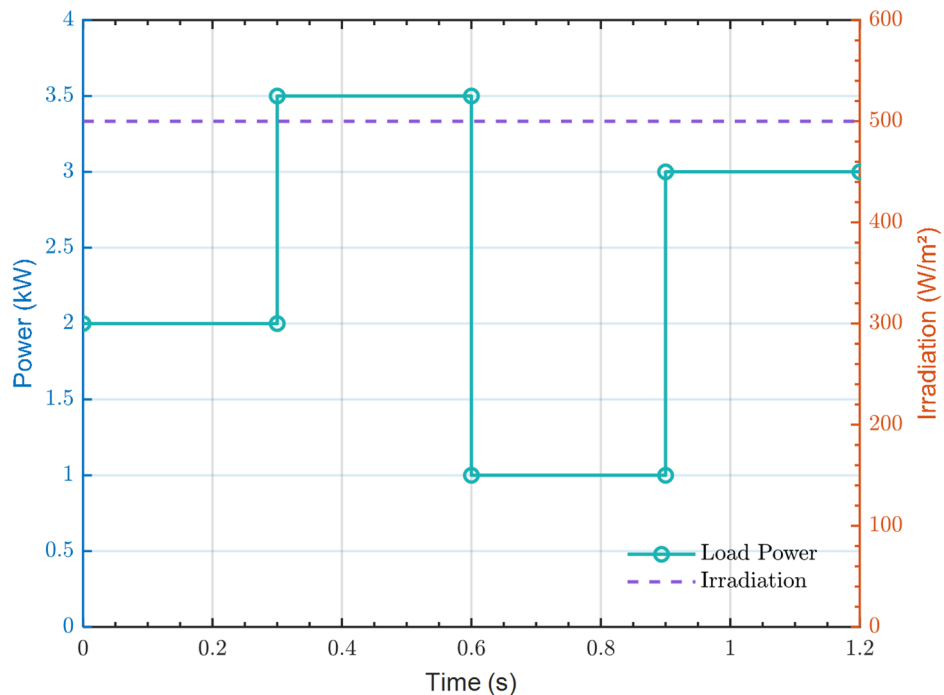


Fig. 22. Test profiles under step changes in load demand with constant PV irradiation and temperature.

to 3 kW. It can be clearly seen that the PV power curve is a straight line of approximately 1.8 kW because the irradiance is fixed, confirming the precision of the MPP tracking algorithm. At the same time, the power curve of the HESS shows that high-frequency power is handled by the supercapacitor and low frequencies are handled by the batteries. The findings confirm that the proposed approach efficiently accommodates both gradual and sudden load demand variations, thereby alleviating stress on the batteries and prolonging their lifespan.

Figure 23b depicts the DC microgrid bus voltage, which shows that the proposed NHGO with PI control strategy limits the DC microgrid bus voltage deviation to ± 2 V, corresponding to an overshoot/undershoot of approximately 0.5% relative to 400 V. The stabilization time is approximately of 30–35 ms, after which the voltage resumes its nominal value with steady-state error < 0.4 V (around 0.1%). This demonstrates that the proposed approach successfully maintained the microgrid voltage at its setpoint value while handling disturbances and variations caused by load demand, thus confirming the efficacy of the proposed approach.

The BDDC-based battery and BDDC-based supercapacitor input current responses, shown in Fig. 23c and d, confirm effective power allocation among the HESS components, in which the supercapacitor current peaks at approximately 2.8 A during the transient, quickly compensating the instantaneous power deficit, while the battery current increases more slowly from 0.9 A to 1.5 A to cover the long-term load. After approximately 40 ms, both currents converge to their new steady-state values. The absence of oscillation or residual ripple highlights the superior damping provided by the NHGO.

Figure 24a and b present respectively the state of charge for the batteries and supercapacitor, revealing that they charge and discharge in response to sudden load demands within their acceptable operating range. The

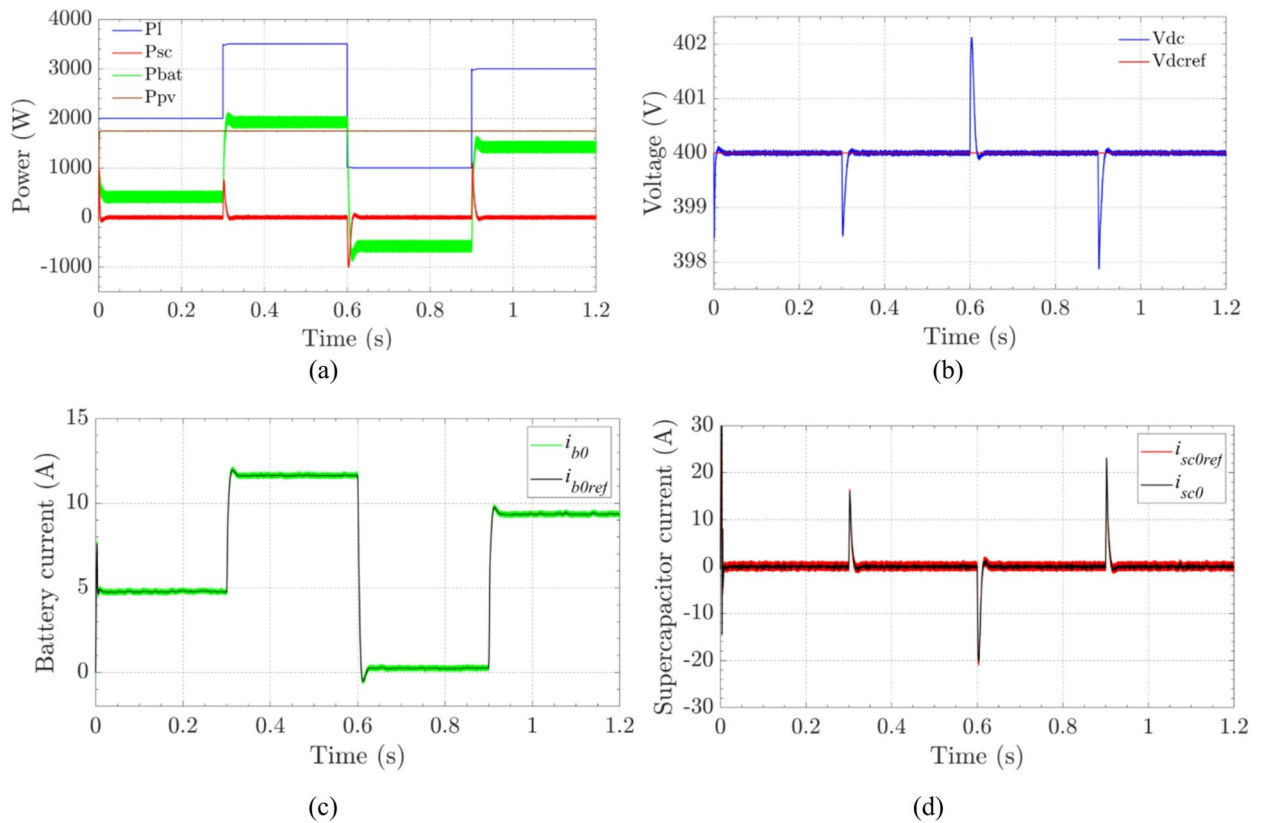


Fig. 23. Simulation results under step changes in load demand (a) Different power of the DC microgrid components, (b) DC bus voltage, (c) BDDC-based battery input current, and (d) BDDC-based supercapacitor input current.

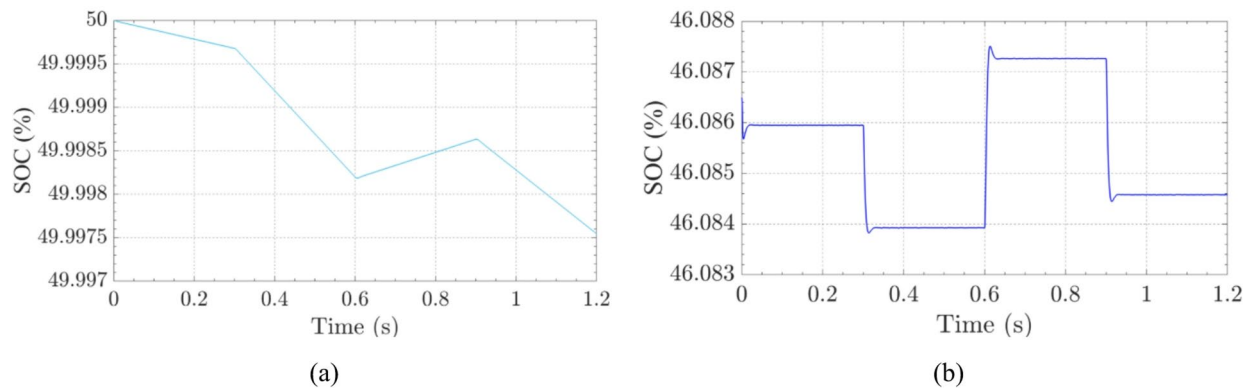


Fig. 24. State of charge (a) Battery. (b) Supercapacitor.

findings validate the proposed strategy’s ability to sustain the DC microgrid bus voltage level and enhance disturbance rejection while ensuring excellent power allocation, even under fluctuating load demands.

The estimated disturbance results presented in Fig. 25 clearly demonstrate the high accuracy and fast convergence capability of the proposed NHGO when estimating external disturbances under different operating conditions of the DC microgrid. Under irradiation variations (Fig. 25a), the observer exhibits a very rapid response, with a minimal overshoot of approximately 0.22% and a short stabilization time of about 20 ms, while the steady-state estimation error is nearly zero. During temperature fluctuations (Fig. 25b), the NHGO maintains a smooth dynamic response characterized by a slightly higher overshoot of 0.25% and a settling time of around 25 ms, again achieving negligible steady-state error (<0.1 V). Under load changes (Fig. 25c), which introduce more abrupt disturbances, the observer remains stable and accurate, showing an overshoot of only 0.5%, a stabilization time below 35 ms, and a small residual error of approximately 0.4 V. These quantitative outcomes confirm that the NHGO effectively balances fast disturbance estimation with high noise immunity, achieving

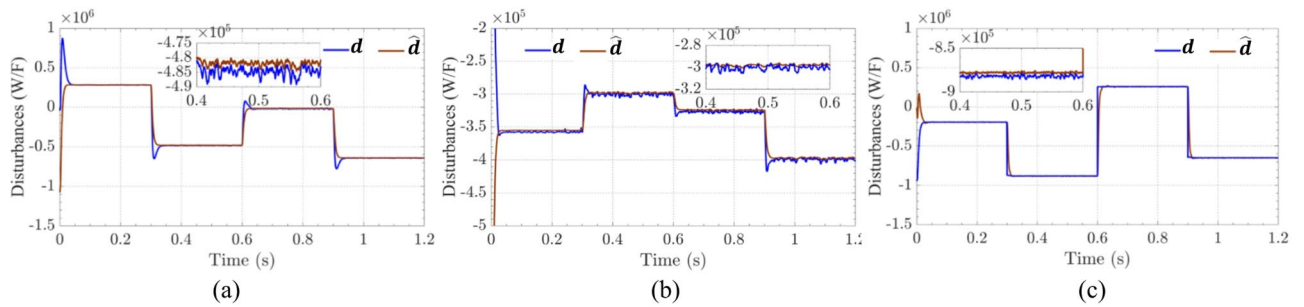


Fig. 25. NHGO estimated disturbance with its actual state. (a) Under changes of irradiation, (b) Under temperature variations, and (c) Under load changes.

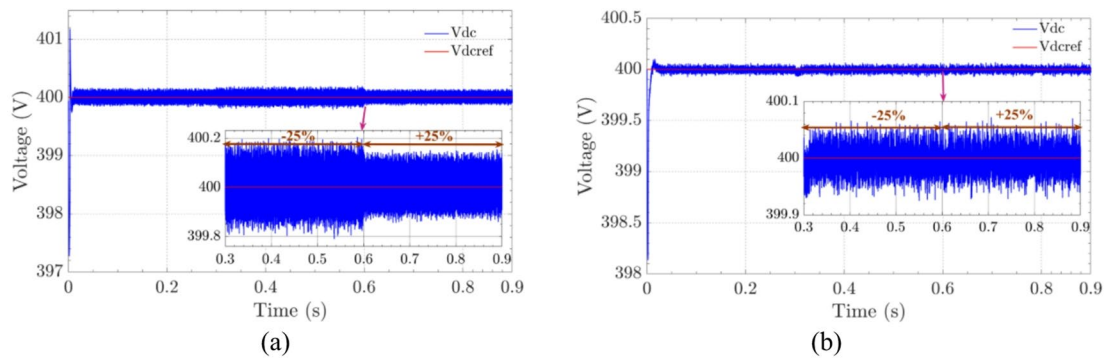


Fig. 26. DC microgrid bus voltage (a) Under varying DC capacitance. (b) Under varying inductance.

rapid transient convergence and minimal steady-state deviation across all tested conditions. The adaptive gain mechanism of the NHGO allows it to provide swift disturbance tracking during transients while maintaining low-gain operation and superior estimation accuracy in steady state.

Performance under parameters change in DC link capacitance and converter's inductance

This scenario aims to evaluate the resilience of the proposed methodology by studying the impact of uncertainty in the DC microgrid bus capacity parameters on the system performance. where, the capacity and inductance values are reduced by 25% from their initial values and then increased by 25%. Figures bellow shows the DC microgrid bus voltage, with the DC microgrid bus voltage curve for a variation in the DC microgrid bus capacitance in Fig. 26a and the DC microgrid bus voltage curve for a variation in the inductance value of the converters in Fig. 26b. It is evident that fluctuations in the internal parameters of the microgrid lead to minimal ripples as they do not impact the behavior of the bus voltage, which in turn demonstrates the robustness of the proposed approach to variations in internal parameters.

Comparison with exciting observers-based control methods

This section presents a comparative study of the proposed NHGO-based control method with these existing observer-based control methods for DC microgrid control approaches, incorporating the ESO with PI in⁴⁹, HGO in³⁵, and the modified super twisting observer with PI controller (STO-PI) in^{18,50}.

To ensure a fair comparison among the four observer-based control strategies (ESO-PI, HGO-PI, STO-PI, and the proposed NHGO-PI), all controllers were implemented under identical excitation conditions and system settings. The irradiance, temperature, and load-step profiles used in Fig. 27a and b were identical for all methods. Each control algorithm was executed in MATLAB/Simulink with a fixed simulation step of 6 μ s and a PWM switching frequency of 20 kHz for the three converters within the DC microgrid system. The same system parameters in Tables 1 and 2 were used across all cases. Additionally, the observer's gains of each observer are tuned using the pole placements approach following the methodology in⁴⁴ to achieve comparable dynamic bandwidths. The ESO and HGO observer gains were selected to match the identical steady state of the proposed NHGO, and the STO gain parameters were tuned using the same method to to match the identical dynamics of the proposed NHGO. The PI gains for all voltage and current loops were tuned also using the pole placements approach according to their bandwidths, damping factors, and system parameters and kept identical across all in all control methods as given in Table 3. The computational parity was also verified, in which all simulations were run on the same processor. The average CPU time per integration step and memory usage were recorded to compare algorithmic complexity.

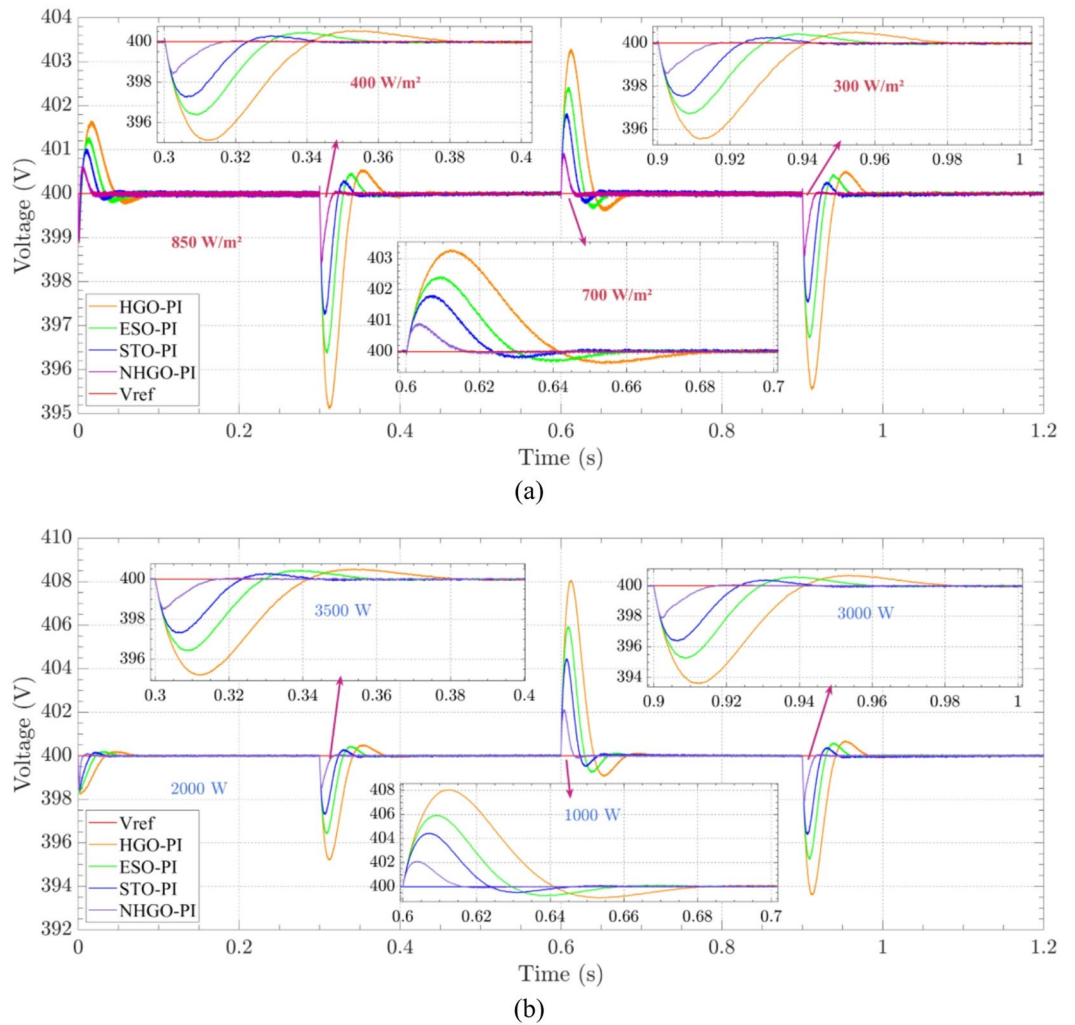


Fig. 27. DC microgrid bus voltage: (a) Under irradiance variation (b) Under load variation.

Method	IAE (%)	OS (%)	T_{dr} (ms)	RMSE (V)	CPU time (s)	Microgrid voltage ripple
ESO in [49]	0.0392	0.59	65	0.0037	20.5593	0.92
HGO in [35]	0.0694	0.79	110	0.0034	20.4498	0.86
STO in [18]	0.0234	0.44	55	0.0039	20.2770	0.8
Proposed NHGO	0.0074	0.22	20	0.0042	20.4416	0.64

Table 3. Comparative performance of observer-based control strategies (ESO, HGO, STO, and proposed NHGO) under identical operating conditions.

All simulations were executed on the same PC (Intel i5-1145G7, 2.6 GHz) to maintain equal computational budgets. For statistical validation, three independent runs were performed for each control method under identical disturbance profiles. The performance indices reported in Table 3 represent the mean with standard deviation across the ten runs.

Results below presents the DC microgrid bus voltage curves for the various techniques. Two scenarios were considered in this study: the Fig. 27a shows the voltage response of the system in the case of a sudden change in irradiance, and the Fig. 27b shows the voltage response of the system in the case of a change in the load demand. Regarding the scenario in Fig. 27a, the irradiation was initially 850 W/m² after a time of 0.3 s, it dropped sharply to 400 W/m², then after the same time interval it rose to 700 W/m² before dropping after a time of 0.9 s to 300 W/m². In this scenario, the undershoot recorded during the first variation in sunlight using the proposed method remained below 1.5 V, whereas for the other methods, it surpassed 2.0 V. In addition, the overshoot recorded during the second variation remained below 1 V, whereas it was well above 2 V for the other methods. These results confirm the superiority of the proposed method in rejecting disturbances, even in the

most challenging environmental conditions. In the scenario in Fig. 27b, the irradiation was fixed, whereas the load demand was initially 2 kW after 0.3 s. The demand suddenly increased to 3.5 kW, and then after the same time interval, it decreased to 1 kW before rising to 3 kW after 0.9 s. In this scenario, the undershoot recorded during the first variation in sunlight using the proposed method remained below 1.5 V, whereas for the other methods, it surpassed 2 V. In addition, the overshoot recorded during the second variation remained below 2.0 V, whereas it was well above 4 V for the other methods. These results confirm the superiority of the proposed method in rejecting disturbances, even in the most challenging load-demand fluctuations.

Table 3 summarizes the performance metrics used to evaluate the different observer-based control methods. The first metric is the Integral Absolute Error (IAE) in (%), which defined as:

$$IAE = \int_0^t \left| \frac{v_{dc}^{2*}}{2} - \frac{v_{dc}^2}{2} \right| dt \quad (72)$$

This metric quantifies the cumulative deviation of the DC microgrid bus voltage from its reference. A smaller IAE indicates more accurate voltage regulation and better tracking performance.

The second metric is DC microgrid voltage overshoot (OS) in (%), which measures the transient peak in the DC microgrid voltage response, in which lower values denote a smoother and more stable convergence to the desired voltage. This metric is expressed by

$$OS = 100 \frac{(v_{dcmax} - v_{dcss})}{v_{dcss}} \quad (73)$$

where v_{dcmax} represent the maximal peak value of the DC microgrid voltage during transient and v_{dcss} represent the steady state value of the DC microgrid voltage.

The third metric is the Disturbance Recovery Time (T_{dr}) (ms), which represents the time required for the system to return to steady state after a disturbance. The smaller T_{dr} corresponds to faster disturbance rejection and enhanced dynamic performance. This metric is expressed by:

$$T_{dr} = t_{ss} - t_{pert} \quad (74)$$

where t_{pert} is the time instant when the disturbance is applied (for example, when a load step or irradiance change occurs), and t_{ss} is the time instant when the system output (DC microgrid voltage, v_{dcss}) returns and remains within a defined steady-state tolerance band after the disturbance.

The fourth metric is the Root Mean Square Error (RMSE) in (V), which represent the square root of the average squared error. The smaller RMSE value means better tracking accuracy and smaller steady-state error. This metric is expressed by:

$$RMSE = \sqrt{\frac{1}{N} \sum_{i=1}^N \left(\frac{v_{dc}^{2*}}{2} - \frac{v_{dc}^2}{2} \right)^2} \quad (75)$$

where i represents the number of sample and N represents the total number of samples.

Finally, the CPU time metric that reflects the average computational load per simulation step, in which the lower CPU time implies higher computational efficiency and better suitability for real-time control implementation.

The results in Table 3 clearly demonstrate the superior performance of the proposed NHGO-PI control scheme compared with the other observer-based methods. The NHGO achieves the lowest Integral Absolute Error (0.0074), confirming its excellent voltage-tracking capability and precise reference regulation. Its overshoot of only 0.22% indicates a smooth transient with minimal voltage fluctuation, while the disturbance recovery time of 20 ms reflects its fast dynamic response and effective disturbance rejection with very lower voltage ripples.

In contrast, the conventional ESO and HGO exhibit larger IAEs (0.0392 and 0.0694, respectively) and significantly slower recovery times (65 ms and 110 ms), mainly due to their fixed-gain structures, which limit adaptability to rapid operating changes. The STO method shows improved performance over ESO and HGO, but it still presents higher overshoot (0.44%) and longer recovery time (55 ms) than the NHGO because of residual chattering effects and tuning complexity.

Despite its enhanced dynamic behavior, the CPU time of the NHGO (≈ 20.44 s) remains comparable to that of the other methods, confirming that the proposed nonlinear adaptive-gain mechanism improves control precision and speed without increasing computational cost. These results collectively validate that the NHGO-based controller offers the best balance among tracking accuracy, disturbance rejection, and real-time implementability for DC microgrid voltage regulation in PV with hybrid energy-storage systems.

Dynamic response and noise sensitivity analysis

To assess the sensitivity of the proposed NHGO-based control approach to measurement noise and to analyze its dynamic response, a simulation study was performed by introducing homogeneous stochastic measurement noise to the measured DC microgrid voltage in the interval of $[-0.2$ V, 0.2 V]. The simulation also includes a sudden load power variation from 2 kW to 3.5 kW at $t=0.3$ s, and the performance of four observers, ESO⁴⁹, HGO³⁵, STO¹⁸, and the proposed NHGO, was evaluated in these conditions.

Figure 28 illustrates the transient responses of the estimated disturbances. Among all evaluated observers, the proposed NHGO exhibits the best performance, responding rapidly to the load step change with a significantly

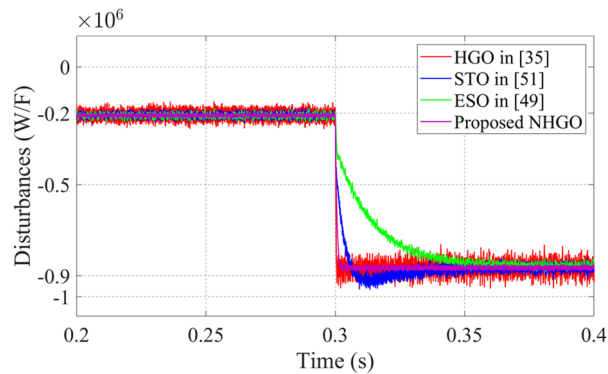


Fig. 28. Estimated disturbance under the presence of noise when the load power is changed from 2 kW to 3.5 kW.

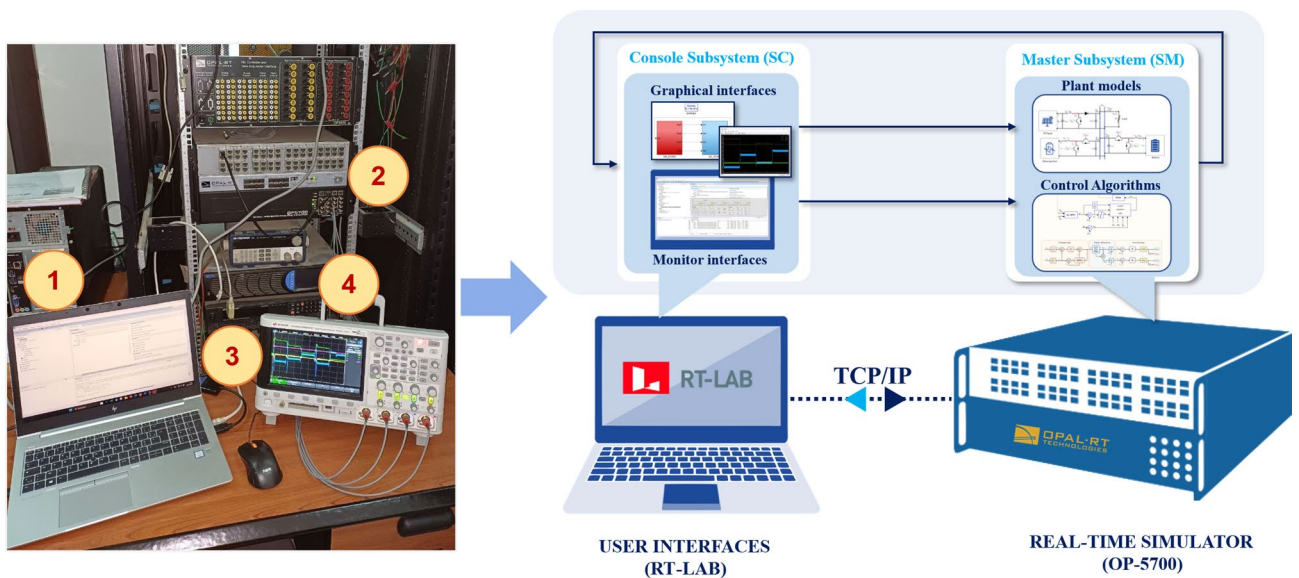


Fig. 29. Structure and working principle of the real-time test bench.

shorter settling time while effectively suppressing measurement noise. This demonstrates its capability in managing the compromise between fast disturbance estimation and noise enhancement inherent in traditional observers. Thanks to the adaptive nonlinear gain mechanism of the proposed NHGO, which achieves an optimal trade-off between estimation speed and noise mitigation, the approach improves disturbance estimation accuracy, dynamic response, measurement noise suppression, and steady-state accuracy. In contrast, the disturbance estimates obtained from the HGO and STO show pronounced ripples. These findings prove that the proposed NHGO achieves the most robust performance in terms of both dynamic response and noise immunity, maintaining minimal steady-state estimation error even in the presence of measurement noise.

Real time implementation and validation

To further evaluate the practical feasibility of the proposed NHGO-PI controller, the OPAL-RT OP5700 system was used to carry out real-time tests, as illustrated in Fig. 29, comprises a PC (01) used to visualize and monitor the overall simulation system in real time. This host communicates with the OP5700 target (02) via the TCP/IP protocol (03). The real-time validation of the proposed NHGO-PI control strategy and the comparative observer-based controllers (ESO-PI, HGO-PI, and STO-PI) was carried out on the OPAL-RT OP5700 hardware-in-the-loop (HIL) platform. All control algorithms were executed on the same computational target using the RT-LAB environment to ensure parity in execution conditions. The simulation solver operated in fixed-step mode with a sampling period of $T_s = 6 \mu\text{s}$. The DC DC converters within the DC microgrid were driven with a PWM switching frequency of $f_s = 20 \text{ kHz}$, synchronized with their corresponding inner current control loops to guarantee consistent duty-cycle updates.

The overall CPU utilization during real-time execution remained between 75% and 80%, confirming that the proposed controller-based DC microgrid control system operates well within the available computational budget. These characteristics ensure faithful emulation of embedded implementation constraints and allow

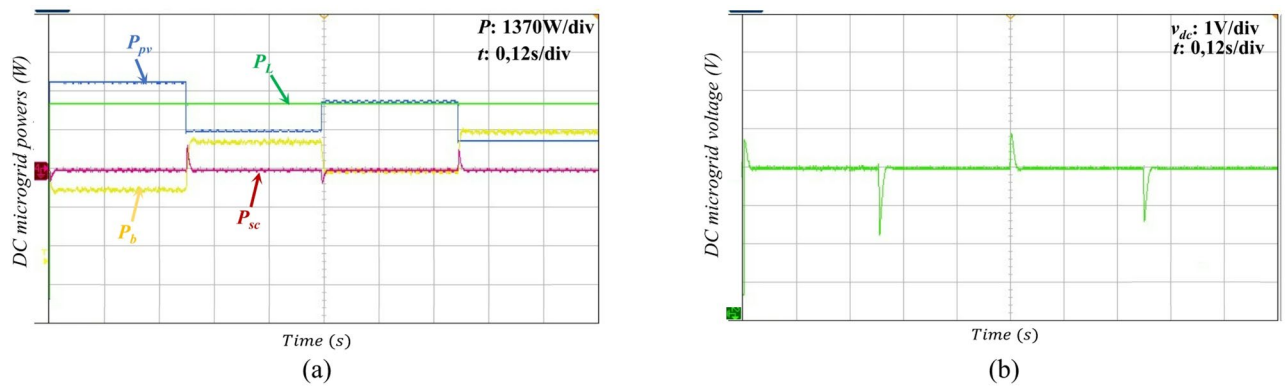


Fig. 30. Real time results under changes in irradiance. (a) Power distribution among DC microgrid components; (b) DC microgrid bus voltage waveform.

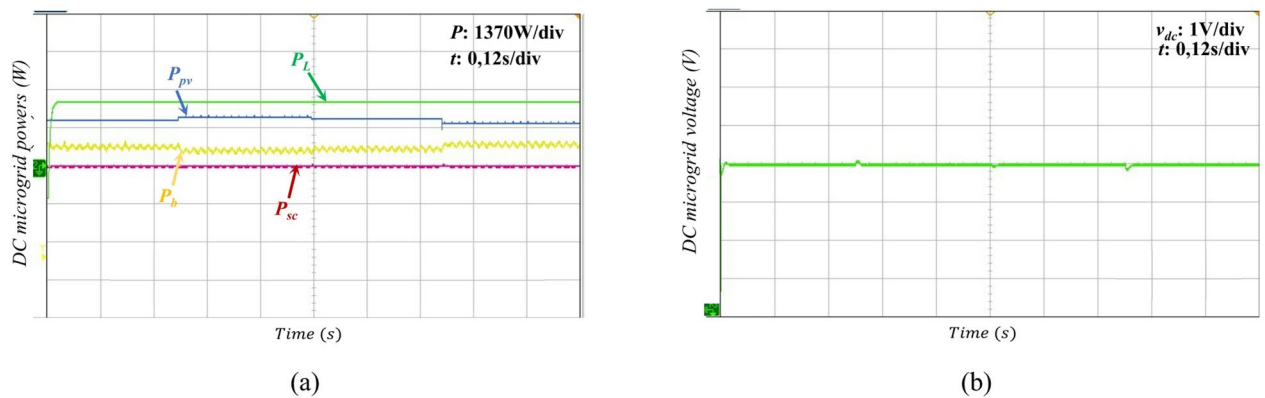


Fig. 31. Real time results under changes in temperature. (a) Power distribution among DC microgrid components; (b) DC microgrid bus voltage waveform.

direct comparison of the dynamic performance and computational efficiency among all observer-based control methods. The real-time tests of the proposed method was carried out under the three following distinct scenarios.

- Scenario 01: Step changes in irradiance and constant load demand and temperature;
 - Scenario 02: Step changes in temperature with constant load demand and irradiance;
 - Scenario 03: Step changes in load demand with constant irradiation and temperature.
- The results of the real-time implementation are shown in Figs. 29, 30, 31 and 32.

Scenario 1: changes in irradiance and constant load demand and temperature

In this scenario, the responsiveness of the proposed control system to sudden changes in solar irradiance was assessed under the assumption of a steady load demand. To guarantee the precision of the real-time simulation, the solar irradiance and load profiles were kept the same as those employed in the previous simulation, as illustrated in Fig. 17. The power response of the real-time simulation of the system under this scenario is presented in Fig. 30a, wherein the load power remained constant, and the PV power effectively tracked the maximum power point. Concurrently, Fig. 30b depicts the DC microgrid voltage response within the same scenario. Peaks were observed during each variation in sunlight. However, these peaks remained within very lower range (approximately 1.7 V). These findings substantiate the effectiveness and feasibility of the proposed approach under irradiance changes.

Scenario 2: changes in temperature with constant load demand and irradiation

This scenario primarily aims to assess the effectiveness of the proposed control strategy, considering the influence of temperature fluctuations in the PV cells on the performance of the microgrid while maintaining a stable load demand. To ensure the accuracy of the real-time validation, the temperature levels and load profiles were aligned with those employed in the previous simulation, as shown in Fig. 20. As shown in Fig. 31a, this temperature fluctuation does not significantly affect the power responses. Figure 31b shows the DC microgrid voltage curve under the same conditions. These findings align with the simulation results, proving the effectiveness and practicality of the proposed approach under PV temperature variations.

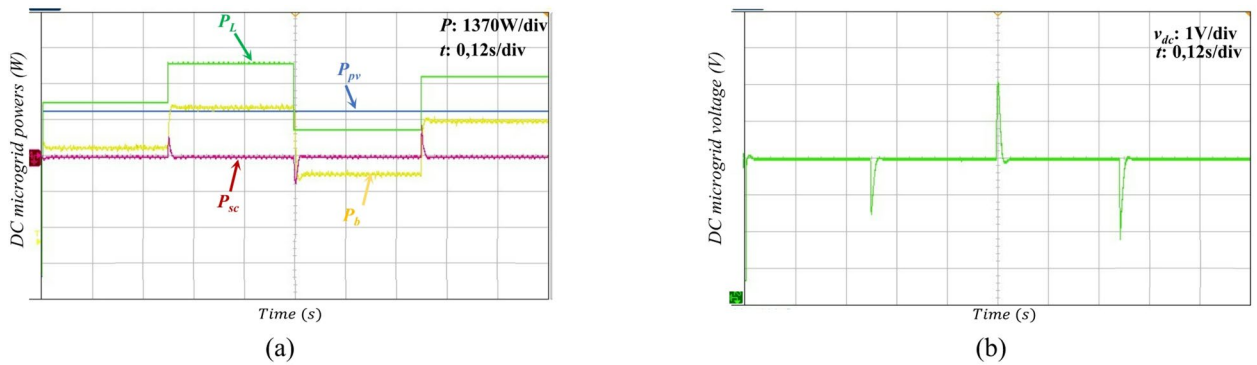


Fig. 32. Real time results under changes in load demand. (a) Power distribution among DC microgrid components; (b) DC microgrid bus voltage waveform.

Scenario 3: changes in load demand with constant irradiation and temperature

This scenario seeks to assess the performance of the microgrid in response to abrupt changes in load demand, while the solar irradiation levels and load profiles were maintained, as shown in Fig. 24. The power response obtained from a real-time system simulation is depicted in Fig. 32a, wherein the solar irradiance was maintained constant, and the load power profile exhibited variability. The results demonstrated an excellent power distribution that was identical to that achieved in the simulation studies. Figure 32b illustrates the voltage response under the same scenario. Voltage peaks were observed for each load-demand variation. However, these transient peaks remained within the acceptable operational limits. These experimental results validate the robustness and practical viability of the proposed control strategy when subjected to variable load demand conditions.

Conclusion

This study presented a NHGO-based control strategy integrated with a PI regulator for effective DC microgrid voltage regulation in photovoltaic-HESSs. By implementing an adaptive gain mechanism, the proposed NHGO enhances both disturbance estimation speed and steady-state accuracy through an adaptive nonlinear gain mechanism. Unlike traditional ESO, HGO, and STO approaches that suffer from the trade-off between fast convergence and noise sensitivity, the NHGO overcomes this limitation by dynamically adjusting its gain to achieve fast disturbance estimation during transients while maintaining noise immunity in steady state.

Comprehensive simulation and real-time experiments confirmed the superior dynamic and steady-state accuracy of the proposed scheme. Quantitatively, the NHGO achieved the lowest IAE of 0.0074, the smallest overshoot of 0.22%, and the fastest disturbance recovery time of 20 ms, compared to ESO (0.0392%, 0.59%, 65 ms), HGO (0.0694%, 0.79%, 110 ms), and STO (0.0234%, 0.44%, 55 ms). The RMSE of the DC microgrid voltage remained within 0.0042 V, confirming excellent voltage tracking precision. The DC microgrid bus voltage deviation was limited to ± 2 V (approximately of 0.5%) even under abrupt load and irradiance changes, with a steady-state error below 0.4 V (0.1%). Furthermore, real-time implementation on the OPAL-RT OP5700 platform demonstrated that the proposed NHGO maintained CPU execution times (approximately of 20.44 s) comparable to existing methods while ensuring fast transient response (< 35 ms) and robust disturbance rejection across all operating scenarios. These improvements are thanks to the adaptive nonlinear gain mechanism of the proposed NHGO, which achieves an optimal balance between disturbance estimation speed, noise mitigation, and steady-state performance, thereby improving voltage regulation accuracy, dynamic responses, disturbance rejection ability, and steady-state performance, as well as excellent power allocation among HESS.

The HESS power coordination results verified that the supercapacitor handled over 80% of transient power, while the battery supplied the steady-state component, effectively reducing current stress and extending storage lifespan. The NHGO's adaptive estimation ensured smooth power-sharing transitions, high stability, and minimal voltage ripple under parameter uncertainties ($\pm 25\%$ variations in capacitance and inductance).

In summary, the proposed NHGO-PI control method significantly improves DC microgrid voltage regulation, achieving a balance between speed, precision, and computational efficiency. Its robustness against environmental disturbances and internal parameter uncertainties makes it a promising candidate for real-time embedded control in renewable-based DC microgrids.

Data availability

The datasets used and/or analyzed during the current study available from the corresponding author on reasonable request.

Appendix: Closed-loop convergence and stability analysis of NHGO with PI controller

This section presents a rigorous stability and convergence analysis of the proposed NHGO integrated with a PI regulator for DC microgrid bus voltage regulation. As illustrated in Fig. 3, the PI controller output directly influences the input $u_c = P_{HESS}^*$ in the NHGO dynamics, creating a feedback interconnection whose stability properties must be carefully analyzed. We demonstrate asymptotic stability, exponential convergence properties,

robustness characteristics, and disturbance rejection capabilities of the closed-loop system under time-varying and transient disturbances. The analysis employs a Piecewise Quadratic Lyapunov Function (PQLF) approach to handle the saturation nonlinearity inherent in the NHGO design⁵¹.

To establish rigorous stability guarantees, we first state the assumptions (1–5) under which the subsequent analysis holds.

According to the PI controller law defined in Eq.(47), the integral state evolves as:

$$\dot{\vartheta} = K_{iv} (x^* - \hat{x}_1 - x + \hat{x}_1) = k_{idc} (e_v - e_1) = K_{iv} e_{pi} \tag{A.1}$$

where the PI tracking error is defined as:

$$e_{pi} = e_v - e_1 \tag{A.2}$$

From Eqs. (19), (26), and (A.1), the augmented error dynamics (AEDs) system incorporating both observer and controller states can be expressed as:

$$\begin{cases} \dot{e}_1 = e_2 - \frac{\beta_1}{k_1} e_1 - \frac{\beta_1 f (k_1 - k_2)}{k_1 k_2} \text{sat} \left(\frac{e_1}{f} \right) + \frac{K_{pv}}{C_{dc}} e_1 \\ \dot{e}_2 = d - \frac{\beta_2}{k_1^2} e_1 - \frac{\beta_2 d (k_1^2 - k_2^2)}{(k_1^2 - k_2^2)^2} \text{sat} \left(\frac{e_1}{f} \right) + \frac{K_{iv}}{C_{dc}} e_1 \\ \dot{\vartheta} = K_{iv} (e_v - e_1) \end{cases} \tag{A.3}$$

To analyse the closed-loop system stability, we employ the following Piecewise Quadratic Lyapunov Function (PQLF) that accounts for both observer and controller states:

$$V_{cl}(e_1, e_2, \vartheta) = V(e_1, e_2) + \sigma \vartheta^2 = e^T P e + \sigma \vartheta^2 \tag{A.4}$$

where $P = \begin{bmatrix} p_{11} & p_{12} \\ p_{21} & p_{22} \end{bmatrix}$ is a symmetric positive definite matrix and $\sigma > 0$ is a weighting coefficient. The specific form of V_{cl} (either V_{cl1} or V_{cl2}) depends on the region of the state space. Expanding the PQLF in Eq.(A.4) yields:

$$V_{cl}(e) = p_{11} e_1^2 + 2p_{12} e_1 e_2 + p_{22} e_2^2 + \sigma \vartheta^2 \tag{A.5}$$

The derivative of V_{cl} along the system trajectories is:
Along the system trajectories, the time derivative of V_{cl} is:

$$\dot{V}_{cl}(e_1, e_2, \vartheta) = (2p_{11} e_1 + 2p_{12} e_2) \dot{e}_1 + 2\sigma \vartheta \dot{\vartheta} + (2p_{12} e_1 + 2p_{22} e_2) \dot{e}_2 \tag{A.6}$$

Assumption 6 The Lyapunov function $V_{cl}(e)$ and its derivative $\dot{V}_{cl}(e)$ are continuous at the boundary $|e_1| = f$. This assumption is satisfied by construction, as both $V_{cl}(e)$ (being quadratic) and the saturation function (being continuous) ensure continuity at the switching boundary.

The presence of the saturation function in the error dynamics necessitates a piecewise analysis approach. Following the approach established in^{52,53}, we partition the state space into two distinct regions based on the magnitude of $\frac{|e_1|}{f}$ as follows:

Linear Region: When $\frac{|e_1|}{f} < 1$, in this region the saturation behaves linearly and $\text{sat} \left(\frac{e_1}{f} \right) = \frac{e_1}{f}$.

Dynamic Region: When $\frac{|e_1|}{f} > 1$, in this region the saturation saturates and $\text{sat} \left(\frac{e_1}{f} \right) = \text{sign} \left(\frac{e_1}{f} \right)$.

This partitioning allows us to analyse the stability using appropriate PSLFs for each region while ensuring global stability through continuity at the boundary.

In Linear Region, by substituting $\text{sat} \left(\frac{e_1}{f} \right) = \frac{e_1}{f}$ into Eq.(A.3), the AEDs system in Eq.(A.3) is simplify to:

$$\begin{cases} \dot{e}_1 = e_2 - \frac{\beta_1}{k_2} e_1 + \frac{K_{pv}}{C_{dc}} e_1 \\ \dot{e}_2 = d - \frac{\beta_2}{k_2^2} e_1 + \frac{K_{iv}}{C_{dc}} e_1 \\ \dot{\vartheta} = K_{iv} (e_v - e_1) \end{cases} \tag{A.7}$$

By substituting the linear region dynamics Eq.(A.7) into Eq.(A.6), we have:

$$\dot{V}_{cl1}(e_1, e_2, \vartheta) = (2p_{11} e_1 + 2p_{12} e_2) \left(e_2 - \frac{\beta_1}{k_2} e_1 + \frac{K_{pv}}{C_{dc}} e_1 \right) + (2p_{12} e_1 + 2p_{22} e_2) \left(d - \frac{\beta_2}{k_2^2} e_1 + \frac{K_{iv}}{C_{dc}} e_1 \right) + 2\sigma K_{iv} (e_v - e_1) \vartheta \tag{A.8}$$

Equation (A.8) can be compactly expressed in matrix form as in Eq.(A.9):

$$\dot{V}_{cl1}(e) = e^T Q_{cl1} e + (2p_{12} e_1 + 2p_{22} e_2) d + 2\sigma K_{iv} (e_v - e_1) \vartheta \tag{A.9}$$

where the matrix Q_{cl1} in Eq.(A.9) is defined by:

$$Q_{cl1} = \begin{bmatrix} q_{cl11} & q_{cl12} \\ q_{cl21} & q_{cl22} \end{bmatrix} \tag{A.9}$$

with elements: $q_{cl11} = -2p_{11} \frac{\beta_1}{k_2} - 2p_{12} \frac{\beta_2}{k_2^2} + 2p_{11} \frac{K_{pv}}{C_{dc}} + 2p_{12} \frac{K_{iv}}{C_{dc}}$,
 $q_{cl12} = p_{11} - p_{12} \frac{\beta_1}{k_2} + p_{12} \frac{K_{pv}}{C_{dc}} + p_{22} \frac{K_{iv}}{C_{dc}} - p_{22} \frac{\beta_2}{k_2^2}$, $q_{cl21} = p_{11} - p_{12} \frac{\beta_1}{k_2} + p_{12} \frac{K_{pv}}{C_{dc}} + p_{22} \frac{K_{iv}}{C_{dc}} - p_{22} \frac{\beta_2}{k_2^2}$,
 and $q_{cl22} = 2p_{12}$. Note that $q_{cl22} = 2p_{12}$, confirming the symmetry of Q_{cl1} .
 Using the Young's inequality with small constant parameter $\epsilon > 0$ to bound the non-quadratic disturbance and integral terms, the term $(2p_{12}e_1 + 2p_{22}e_2)d$ in Eq.(A.9) can be expressed by:

$$2(p_{12}e_1 + p_{22}e_2)d \leq \frac{1}{2\epsilon} (p_{12}e_1 + 2p_{22}e_2)^2 + \frac{\epsilon}{2} d^2 \tag{A.10}$$

Expanding the squared term, Eq.(A.11) can be rewritten as follows:

$$(p_{12}e_1 + 2p_{22}e_2)d \leq \frac{2}{\epsilon} (p_{12}^2e_1^2 + 2p_{12}p_{22}e_1e_2 + p_{22}^2e_2^2) + \frac{\epsilon}{2} d_{max}^2 \tag{A.11}$$

where d_{max} represents the bounded disturbance magnitude $|d| \leq d_{max}$.
 Assuming the voltage tracking error e_v is bounded such that $|e_v| \leq e_{vmax}$, the terms $2\sigma K_{iv}e_v\partial$ is expressed as:

$$2\sigma K_{iv}e_v\partial \leq 2\sigma K_{iv}e_{vmax}|\partial| \leq \sigma K_{iv}^2e_{vmax}^2\partial + \sigma\partial^2 \tag{A.12}$$

Additionally, using the Young's inequality as in Eq.(A.11), the terms $2\sigma K_{iv}e_1\partial$ is expressed as:

$$2\sigma K_{iv}e_1\partial \leq \sigma K_{iv}^2e_1^2 + \sigma\partial^2 \tag{A.13}$$

Combining the terms in Eqs.(A.12), (A.13), and (A.14), the derivative of the PQLF in Eq.(A.9) can be rewritten by:

$$\dot{V}_{cl1}(e) = e^T(Q_{cl1} + Q_\epsilon)e + \frac{\epsilon}{2}d_{max}^2 + \sigma K_{iv}^2e_{vmax}^2 + 2\sigma\partial^2 \tag{A.14}$$

where Q_ϵ , represents the additional positive semi-definite contribution from the bounding procedure, which given by:

$$Q_\epsilon = \begin{bmatrix} \frac{2}{\epsilon}p_{11}^2 & \frac{2}{\epsilon}p_{12}p_{22} \\ \frac{2}{\epsilon}p_{12}p_{22} & \frac{2}{\epsilon}p_{22}^2 \end{bmatrix} \tag{A.15}$$

For closed loop PI with NHGO stability in linear region, we need to choose parameters such that $Q_{cl1} + Q_\epsilon$ is negative definite and the additional constant terms are dominated by the negative quadratic form for large enough errors. The matrix is given as in Eq. (A.17):

$$Q'_{cl1} = \begin{bmatrix} q_{11} & q_{12} \\ q_{21} & q_{22} \end{bmatrix} \tag{A.17}$$

where $q_{11} = -2p_{11}(\frac{\beta_1}{k_2} + \frac{K_{pv}}{C_{dc}}) - 2p_{12}(\frac{\beta_2}{k_2^2} + \frac{K_{iv}}{C_{dc}}) + \frac{2}{\epsilon}p_{12}^2$, $q_{12} = p_{11} - p_{12}(\frac{\beta_1}{k_2} + \frac{K_{pv}}{C_{dc}}) - p_{22}(\frac{\beta_2}{k_2^2} + \frac{K_{iv}}{C_{dc}}) + \frac{2}{\epsilon}p_{12}p_{22}$,

For stability of the closed loop PI with NHGO system in region 1, Q'_{cl1} must be negative definite, which requires to meet the following conditions:

$$\begin{cases} 2p_{11} \left(\frac{\beta_1}{k_2} + \frac{K_{pv}}{C_{dc}} \right) + 2p_{12} \left(\frac{\beta_2}{k_2^2} + \frac{K_{iv}}{C_{dc}} \right) - \frac{2}{\epsilon}p_{12}^2 < 0 \\ 2p_{12} + \frac{2}{\epsilon}p_{22}^2 > 0 \\ \det(Q'_{cl1}) > 0 \end{cases} \tag{A.18}$$

When conditions Eq.(A.18) are satisfied, we obtain:

$$\dot{V}_{cl1}(e) \leq -\min(Q'_{cl1})e^2 + \frac{\epsilon}{2}d_{max}^2 + \sigma K_{iv}^2e_{vmax}^2 + 2\sigma\partial^2 \tag{A.19}$$

where $\lambda_{min}(Q'_{cl1})$ denotes the smallest eigenvalue of Q'_{cl1} . This value set a lower bound on the exponential convergence rate of the estimation error dynamics, which defines the closed loop convergence and robustness of the suggested NHGO with PI controller. A larger value of $\lambda_{min}(Q'_{cl1})$ indicates faster convergence and higher robustness of the suggested NHGO with PI to time-varying dynamics. By appropriately choosing the design parameters (β_1 , β_2 , ρ_2 , k_{pdc} , and k_{idc}), we ensure that the negative definite term $\lambda_{min}(Q'_{cl1})$ dominates the bounded disturbance terms $\frac{\epsilon}{2}d_{max}^2 + \sigma k_{idc}^2e_{vmax}^2 + 2\sigma\partial^2$ for sufficiently large errors. When these conditions are met, $\dot{V}_{obs1}(e) < 0$ for all $e \neq 0$ in region 1, guaranteeing asymptotic stability of the pro-

posed NHGO with PI controller four DC microgrid bus voltage regulation in first region (linear region) while providing faster convergence and higher robustness in the presence of time-varying or transient disturbance dynamics. Additionally, this provides a quantitative resilience threshold against exogenous perturbations and unmodeled dynamics.

Similarly, for the dynamic region (when $\text{sat}(\frac{e_1}{f}) = \text{sign}(\frac{e_1}{f})$), the AEDs system in Eq.(A.3) can be written as:

$$\begin{cases} \dot{e}_1 = e_2 - \frac{\beta_1}{k_1} e_1 - \frac{\beta_1 f(k_1 - k_2)}{k_1 k_2} \text{sign}(\frac{e_1}{f}) + \frac{K_{pv}}{C_{dc}} e_1 \\ \dot{e}_2 = d - \frac{\beta_2}{k_1^2} e_1 - \frac{\beta_2 f(k_1^2 - k_2^2)}{k_1^2 k_2^2} \text{sign}(\frac{e_1}{f}) + \frac{K_{iv}}{C_{dc}} e_1 \\ \dot{\partial} = K_{iv} (e_v - e_1) \end{cases} \quad (A.20)$$

Substituting these AEDs into Eq.(A.6) and following similar bounding procedures as in linear region, we obtained the derivative of the PQLF ($\dot{V}_{cl2}(e)$) corresponding to the dynamic region as follows:

$$\dot{V}_{cl2}(e) = e^T (Q_{cl2} + Q_\epsilon) e + K_{\text{sign}} \text{sign}(e_1) + \frac{\epsilon}{2} d_{\text{max}}^2 + \sigma K_{iv}^2 e_v^2_{\text{max}} + 2\sigma \partial^2 \quad (A.21)$$

where $Q_{cl2} = Q_{cl1}$.

The term $K_{\text{sign}} \text{sign}(e_1)$ represents the collective contribution of all sign function terms. This term can be bound using a combination of Young's and Cauchy-Schwarz inequalities as follows^{51,54}:

$$\psi_{\text{sign}} \text{sign}(e_1) \leq \frac{1}{2} \psi_1^2 + \frac{1}{2} e_1^2 + \psi_2^2 e_2^2 \quad (A.22)$$

For this term to contribute to the stability of the proposed NHGO with PI controller in the dynamic region, ψ_1 and ψ_2 should be negative, which happens if $p_{11} > 0$, $p_{12} > 0$, $p_{22} > 0$, and $k_1 > k_2$, and f should be selected based on the expected amplitude of e_1 . Accordingly, and when appropriate parameter selection, $\dot{V}_{cl2}(e)$ in Eq.(A.21) can be expressed as in Eq.(A.23).

$$\dot{V}_{cl2}(e) \leq -\min(Q_{cl2} + Q_\epsilon) \|e\|^2 + \psi_{\text{sign}} \text{sign}(e_1) + \frac{\epsilon}{2} d_{\text{max}}^2 + \sigma K_{iv}^2 e_v^2_{\text{max}} + 2\sigma \partial^2 \quad (A.23)$$

For overall stability of the proposed NHGO with PI regulator in the dynamic region, we need to choose $p_{11}, p_{12}, p_{22} > 0$ to ensure $Q_{cl2} + Q_\epsilon < 0$, and we select $\beta_1, \beta_2, K_{pv}, K_{iv}, \psi_1$, and ψ_2 sufficient such that the negative definiteness of $e^T (Q_{cl2} + Q_\epsilon) e + K_{\text{sign}} \text{sign}(e_1)$ dominates positive terms $\frac{\epsilon}{2} d_{\text{max}}^2 + \sigma K_{iv}^2 e_v^2_{\text{max}} + 2\sigma \partial^2$. Also, it needs to selecting $k_1 > k_2 > 0$, to provide additional stability margin for large $|e_1|$. When these conditions are satisfied, $\dot{V}_{cl2}(e) < 0$ for all $e \neq 0$ in the dynamic region, guaranteeing closed loop asymptotic stability of the proposed NHGO with PI controller in the dynamic region while providing robustness against the nonlinear dynamics of d .

When the stability conditions in both linear and dynamic regions are simultaneously satisfied, the proposed NHGO with PI regulator system will demonstrate asymptotic stability in both regions, bounded estimation errors even with nonlinear dynamics, reduced peaking phenomenon compared to standard high gain observers, and robustness against model uncertainties. The analysis proves that the estimation errors converge exponentially to zero, and the magnitude of these limits depends on the system uncertainty bounds and the choice of NHGO parameters. Furthermore, the time-scale separation between the NHGO and PI controller dynamics ensures that the closed-loop system remains stable when the estimated states are used for feedback control in the PI controller.

Additionally, the estimation errors e_1, e_2 converge exponentially with a convergence rate determined by⁵⁵:

$$\|e(t)\| \leq \|e(0)\| e^{\left(-\frac{\min(Q'_{cl1})}{2 \max(P)} t\right)} \quad (A.24)$$

where $\lambda_{\text{max}}(P)$ is the largest eigenvalue of matrix P . Accordingly, the convergence time constant is given approximately by⁵⁵:

$$T_{\text{conv}} \approx \frac{2 \max(P)}{\min(Q'_{cl1})} \quad (A.25)$$

Received: 4 September 2025; Accepted: 27 November 2025

Published online: 18 December 2025

References

- Xiao, J., Wang, P. & Setyawan, L. Hierarchical control of hybrid energy storage system in DC microgrids. *IEEE Trans. Industr. Electron.* **62** (8), 4915–4924 (2015).
- Jing, W., Hung Lai, C., Wong, S. H. W. & Wong, M. L. D. Battery-supercapacitor hybrid energy storage system in standalone DC microgrids: A review. *IET Renew. Power Gener.* **11** (4), 461–469 (2017).
- Kotra, S. & Mishra, M. K. Design and stability analysis of DC microgrid with hybrid energy storage system. *IEEE Trans. Sustain. Energy.* **10** (3), 1603–1612 (2019).

4. Justo, J. J., Mwasilu, F., Lee, J. & Jung, J. W. AC-microgrids versus DC-microgrids with distributed energy resources: A review. *Renew. Sustain. Energy Rev.* **24**, 387–405 (2013).
5. Lotfi, H. & Khodaei, A. AC versus DC microgrid planning. *IEEE Trans. Smart Grid.* **8** (1), 296–304 (2017).
6. Sinha, S. & Bajpai, P. Power management of hybrid energy storage system in a standalone DC microgrid. *J. Energy Storage.* **30**, 101523 (2020).
7. Kumar, D., Zare, F. & Regulations, . Regulations a comprehensive review of maritime microgrids: system architectures, energy efficiency, power quality. *IEEE Access* **7**, 67249–67277 (2019).
8. Xu, Q. et al. Review on advanced control technologies for bidirectional DC/DC converters in DC microgrids. *IEEE J. Emerg. Sel. Top. Power Electron.* **9** (2), 1205–1221 (2021).
9. Ihammouchen, S. *1st International Conference on Circuits, Power and Intelligent Systems (CCPIS)*, IEEE, Sep. 2023, pp. 1–6. (2023). <https://doi.org/10.1109/CCPIS59145.2023.10291421>
10. Hajiaghahi, S., Salemnia, A. & Hamzeh, M. Hybrid energy storage system for microgrids applications: A review. *J. Energy Storage.* **21**, 543–570 (2019).
11. Chebabhi, A. et al. Enhanced grid current and DC voltage regulations for three level four leg rectifier DC microgrid under uncertainty and disturbances. *Sci. Rep.* **15** (1), 23938 (2025).
12. Faisal, M. et al. Review of energy storage system technologies in microgrid applications: issues and challenges. *IEEE Access.* **6**, 35143–35164 (2018).
13. Amine, H. M., Mouaz, A. K., messaoud, H., Othmane, A. & Saad, M. The impacts of control systems on hybrid energy storage systems in remote DC-Microgrid system: A comparative study between PI and super twisting sliding mode controllers. *J. Energy Storage.* **47**, 103586 (2022).
14. Zhang, X., Wang, B., Gamage, D. & Ukil, A. Model predictive control based dynamic power loss prediction for hybrid energy storage system in DC microgrids. *IEEE Trans. Industr. Electron.* **69** (8), 8080–8090 (2022).
15. Wu, M., Lu, D. D. C. & Tse, C. K. Direct and optimal linear active methods for stabilization of LC input filters and DC/DC converters under voltage mode control. *IEEE J. Emerg. Sel. Top. Circuits Syst.* **5** (3), 402–412 (2015).
16. Elwarfalli, H., Muntaser, A., Kumar, J. & Subramanyam, G. Design and implementation of PI controller for the hybrid energy system, in *2016 IEEE National Aerospace and Electronics Conference (NAECON) and Ohio Innovation Summit (OIS)*, IEEE, Jul. pp. 170–172. (2016).
17. Hosseinipour, A. & Hojabri, H. Small-signal stability analysis and active damping control of dc microgrids integrated with distributed electric springs. *IEEE Transactions on Smart Grid* **11**(5), 3737–3747 (2020).
18. Wang, B. et al. Higher order sliding mode observer based fast composite backstepping control for HESS in DC microgrids. *IEEE Trans. Sustain. Energy.* **15** (3), 1627–1639 (2024).
19. Ni, F. et al. Enhancing resilience of DC microgrids with model predictive control based hybrid energy storage system. *Int. J. Electr. Power Energy Syst.* **128**, 106738 (2021).
20. Duan, J. et al. Reinforcement-Learning-Based optimal control of hybrid energy storage systems in hybrid AC–DC microgrids. *IEEE Trans. Industr. Inf.* **15** (9), 5355–5364 (2019).
21. Manandhar, U. et al. Joint control of Three-Level DC–DC converter interfaced hybrid energy storage system in DC microgrids. *IEEE Trans. Energy Convers.* **34** (4), 2248–2257 (2019).
22. Khan, K. A. & Khalid, M. Improving the transient response of hybrid energy storage system for voltage stability in DC microgrids using an autonomous control strategy. *IEEE Access.* **9**, 10460–10472 (2021).
23. Das, D., Madichetty, S., Singh, B. & Mishra, S. Luenberger observer based current estimated boost converter for PV maximum power Extraction—A current sensorless approach. *IEEE J. Photovolt.* **9** (1), 278–286 (2019).
24. Wang, B., Xu, J., Xu, D. & Yan, Z. Implementation of an estimator-based adaptive sliding mode control strategy for a boost converter based battery/supercapacitor hybrid energy storage system in electric vehicles. *Energy. Conv. Manag.* **151**, 562–572 (2017).
25. Yang, B. et al. Applications of battery/supercapacitor hybrid energy storage systems for electric vehicles using perturbation observer based robust control. *J. Power Sources.* **448**, 227444 (2020).
26. Wang, B., Manandhar, U., Zhang, X., Gooi, H. B. & Ukil, A. Deadbeat control for hybrid energy storage systems in DC microgrids. *IEEE Trans. Sustain. Energy.* **10** (4), 1867–1877 (2019).
27. Fallah Ghavidel, H. & Mousavi-G, S. M. Observer-based type-2 fuzzy approach for robust control and energy management strategy of hybrid energy storage systems. *Int. J. Hydrog. Energy.* **47** (33), 14983–15000 (2022).
28. Mansour, M. et al. High-gain observer-based sensorless control of a flywheel energy storage system for integration with a grid-connected variable-speed wind generator. *Soft. Comput.* **24** (14), 10585–10596 (2020).
29. Wang, Y., Zhang, X., Liu, C., Pan, R. & Chen, Z. Multi-timescale power and energy assessment of lithium-ion battery and supercapacitor hybrid system using extended Kalman filter. *J. Power Sources.* **389**, 93–105 (2018).
30. Ali, C. et al. An enhanced active disturbance rejection control scheme for DC voltage regulation in photovoltaic Grid-Connected Four-Leg inverter using a sliding mode observer. *IEEE Access.* **13**, 18623–18643 (2025).
31. Chebabhi, A. et al. 3-D unbalanced coordinate transformation with Super-Twisting control and observation for unbalance and disturbance load voltage mitigations in stand alone Four-Leg inverters. *IEEE Access.* **13**, 70464–70488 (2025).
32. Nerkar, S. S., Londhe, P. S. & Patre, B. M. Design of super twisting disturbance observer based control for autonomous underwater vehicle. *Int. J. Dynamics Control.* **10** (1), 306–322 (2022).
33. Zhou, J. et al. Decentralized robust control for vehicle platooning subject to uncertain disturbances via Super-Twisting Second-Order Sliding-Mode observer technique. *IEEE Trans. Veh. Technol.* **71** (7), 7186–7201 (2022).
34. Bahrami, M., Naraghi, M. & Zareinejad, M. Adaptive super-twisting observer for fault reconstruction in electro-hydraulic systems. *ISA Trans.* **76**, 235–245 (2018).
35. Errouissi, R. & Al-Durra, A. Extended high-gain observer-based DC-link voltage regulation in dual-stage grid-tied PV system under balanced and unbalanced voltages. *IET Renew. Power Gener.* **14** (12), 2037–2046 (2020).
36. Ball, A. A. & Khalil, H. K. Analysis of a nonlinear high-gain observer in the presence of measurement noise, in *Proceedings of the 2011 American Control Conference*, IEEE, Jun. pp. 2584–2589. (2011).
37. Prasov, A. A. & Khalil, H. K. A nonlinear High-Gain observer for systems with measurement noise in a feedback control framework. *IEEE Trans. Autom. Control.* **58** (3), 569–580 (2013).
38. Debdouche, N. et al. Synergetic simplified super-twisting algorithm control for stability enhancement of PV/BESS-based DC microgrid. *Sci. Rep.* **15** (1), 7392 (2025).
39. Mohamed Cherif, D. E. O., Chebabhi, A. & Kessal, A. Improving PV system power using four-leg interleaved boost converter and MPPT based on robust integral linear quadratic control. *J. Power Technol.* **105** (1), 77–89 (2025).
40. Debdouche, N. et al. Nonlinear MPPT techniques to control hybrid power systems. *Sci. Rep.* **14** (1), 18620 (2024).
41. Mishra, J. & Shankar, A. Optimizing wind-PV-battery microgrids for sustainable and resilient residential communities. *Sci. Rep.* **15** (1), 24339 (2025).
42. Hu, Q., Xie, S. & Zhang, J. Data-based power management control for battery supercapacitor hybrid energy storage system in solar DC-microgrid. *Sci. Rep.* **14** (1), 26164 (2024).
43. Liu, J. et al. Sliding mode control of grid-connected neutral-point-clamped converters via high-gain observer. *IEEE Trans. Industr. Electron.* **69** (4), 4010–4021 (2021).
44. Singh, J. K. et al. Active disturbance rejection control of photovoltaic three-phase grid following inverters under uncertainty and grid voltage variations. *IEEE Trans. Power Delivery.* **38** (5), 3155–3168 (2023).

45. Defdaf, M. et al. Enhanced linear state observer-based PLL-less vector-oriented control method for a three-phase PWM rectifier, *International Transactions on Electrical Energy Systems*, vol. no. 1, p. 7191464, 2024. (2024).
46. Zhao, L., Zheng, C., Wang, Y. & Liu, B. A finite-time control for a pneumatic cylinder servo system based on a super twisting extended state observer. *IEEE Trans. Syst. Man. Cybernetics: Syst.* **51** (2), 1164–1173 (2021).
47. Chebabhi, A., Al-dwa, A. A. M., Barkat, S. & Zebiri, F. Backstepping control of a grid-connected four-leg PWM rectifier under both balanced and unbalanced grid conditions. *Int. J. Syst. Assur. Eng. Manage.* **14** (S1), 1–18 (2023).
48. Chebabhi, A., Defdaf, M. & Kessal, A. Design and PIL implementation of a new robust backstepping based low-complexity voltage-oriented control method for four-leg rectifiers. *Int. J. Electr. Power Energy Syst.* **155**, 109676 (2024).
49. Li, X. et al. Observer-based DC voltage droop and current feed-forward control of a DC microgrid. *IEEE Trans. Smart Grid.* **9** (5), 5207–5216 (2017).
50. Thomas, T., Mishra, M. K., Kumar, C. & Liserre, M. Observer based control using super-twisting technique for a PV-Wind-HESS based DC microgrid feeding constant power loads. *IEEE J. Emerg. Sel. Top. Power Electron.* **13** (1), 1018–1028 (2024).
51. Khalil, H. K. *Nonlinear Systems* 3rd edn (Prentice-Hall, 2002).
52. Yuan, D., Ma, X. J., Zeng, Q. H. & Qiu, X. Research on frequency-band characteristics and parameters configuration of linear active disturbance rejection control for second-order systems. *Control Theory Appl.* **30** (12), 1630–1640 (2013).
53. Dai, D., Hu, T., Teel, A. R. & Zaccarian, L. Analysis of systems with saturation/deadzone via piecewise-quadratic Lyapunov functions, in *2007 American Control Conference*, pp. 5822–5827. (2007).
54. Folland, G. B. *Real Analysis: Modern Techniques and their Applications* 2nd edn (Wiley-Interscience, 1999).
55. Astolfi, D. & Marconi, L. A high-gain nonlinear observer with limited gain power. *IEEE Trans. Autom. Control.* **60** (11), 3059–3064 (2015).

Author contributions

Syphax Ihammouchen, Ali Chebabhi, Djamel Ziane: Conceptualization, Methodology, Software, Visualization, Investigation, Writing- Original draft preparation. Toufik Rekioua, Mohamed Fouad Benkhoris, Youcef Belkhi-er: Data curation, Validation, Supervision, Resources, Writing - Review & Editing. Mohit Bajaj, Olena Rubanen-ko: Project administration, Supervision, Resources, Writing - Review & Editing.

Declarations

Competing interests

The authors declare no competing interests.

Additional information

Correspondence and requests for materials should be addressed to M.B. or O.R.

Reprints and permissions information is available at www.nature.com/reprints.

Publisher's note Springer Nature remains neutral with regard to jurisdictional claims in published maps and institutional affiliations.

Open Access This article is licensed under a Creative Commons Attribution-NonCommercial-NoDerivatives 4.0 International License, which permits any non-commercial use, sharing, distribution and reproduction in any medium or format, as long as you give appropriate credit to the original author(s) and the source, provide a link to the Creative Commons licence, and indicate if you modified the licensed material. You do not have permission under this licence to share adapted material derived from this article or parts of it. The images or other third party material in this article are included in the article's Creative Commons licence, unless indicated otherwise in a credit line to the material. If material is not included in the article's Creative Commons licence and your intended use is not permitted by statutory regulation or exceeds the permitted use, you will need to obtain permission directly from the copyright holder. To view a copy of this licence, visit <http://creativecommons.org/licenses/by-nc-nd/4.0/>.

© The Author(s) 2025